Journal Pre-proof

Dynamic mechanical response of damaged alumina AD995

Brendan M.L. Koch, Calvin Lo, Haoyang Li, Tomoko Sano, Jonathan Ligda, James David Hogan

PII: S0955-2219(20)30833-5

DOI: https://doi.org/10.1016/j.jeurceramsoc.2020.10.020

Reference: JECS 13648

To appear in: *Journal of the European Ceramic Society*

Received Date: 6 July 2020

Revised Date: 6 October 2020

Accepted Date: 11 October 2020

Please cite this article as: { doi: https://doi.org/

Dynamic Mechanical Response of Damaged Alumina AD995

Brendan M. L. Koch[1], Calvin Lo[1], Haoyang Li[1], Tomoko Sano[2], Jonathan Ligda[2], James David Hogan[1]

[1] *Department of Mechanical Engineering, the University of Alberta, Edmonton, AB T6G 2R3, Canada, Contacts bmkoch@ualberta.ca and jdhogan@ualberta.ca,*
[2] *Weapons and Materials Research Directorate, Combat Capabilities Development Command Army Research Laboratory, Aberdeen Proving Ground, MD 21005*

Abstract

This paper explores the compressive responses of alumina ceramics subjected to various levels of pre-damage via internal cracking. Pre-damage is achieved by subjecting the samples to thermal shock. Mechanical loading is performed using a load frame for quasi-static strain rates and a Kolsky bar for dynamic strain rates. Digital image correlation is used to obtain two-dimensional strains alongside independently measured applied stresses. Data acquisition used in this study allows for the calculation of apparent elastic moduli as a function of strain. This allows for the study of change in mechanical response with strain, strain-rate, and level of pre-damage. There is a complex interaction between pre-damage and compressive loading, leading to mechanical damage accumulation being divided into three stages rather than a single damage accumulation function. It was also found that shear modulus change was more indicative of physical failure phenomena during loading than Young's modulus or Poisson's ratio changes.

Keywords: ceramics, damage accumulation, thermal shock, DIC, failure, compressive loading

1. Introduction

There are two distinct but related phenomena tied to the concept of damage in materials, especially for brittle ceramics. The first is physical damage, which is all of the changes to a material that physically manifest such as cracks[1–6], phase change [7–11], twinning[12,13], and comminution [14–18]. Post-mortem analysis[14,19–22] is often used to determine the extent of physical damage after a loading event, and under quasi-static loading, *in situ* X-ray imaging is possible[23–26]. When the material is transparent[27–29], or allows coherent X-rays to pass through the sample such as with single crystal materials[30], physical damage propagation can be studied under dynamic loading conditions. In contrast to physical damage, the second type of damage is what we define as mechanical damage, which is how physical damage manifests as apparent changes in mechanical properties. This can be a change in material failure strength[22,31–34], fracture toughness[35–39], or the speed of sounds in the material[40–44] that relate to elastic constants such as Young's modulus and Poisson's ratio. A primary distinction between physical and mechanical damage is in how they are measured, in that physical damage is present regardless of loading and typically characterized via imaging, while mechanical loading is required to characterize mechanical damage. Due to the fact that physical damage causes mechanical damage, can be measured directly, and does not need a load to be applied, it is desirable to be able to derive mechanical damage behavior from observed physical damage in order to predict how materials will react to loading. Past models have predicted the macroscopic response of brittle materials by taking into account the effects of a single crack [1,2,45,46] or the interaction of multiple cracks[3,4,47–49], but only using the initial flaw population, which is a measure of physical damage, and has had as model inputs has had limited success in simulating the mechanical damage observed in experiments[50,51]. More research into the relationship between physical and mechanical damage is needed.

In brittle materials, physical damage is considered an irreversible process, as once a crack is present, the crack faces will not fuse together again[1–3,45,46]. However, physical damage does not translate to mechanical damage linearly or even monotonically[52–54]. For example, in the study of quasi-brittle rocks associated with seismic faults by Aben *et al.*[52], there was a region where pulverized rock demonstrated higher wave speeds, and thus higher elastic moduli, than

less damaged rocks that were merely fractured. In another study, Shea and Hanson[54] showed that wave speeds in coal samples under compression did not demonstrate linear or monotonic change during the failure process. Building upon previous work with brittle materials under quasi-static and dynamic loading, Koch *et al.*[55] used ultra-high-speed (UHS) photography and digital image correlation (DIC) in conjunction with a Kolsky bar apparatus as outlined by Lo *et al.*[56] to study mechanical damage accumulation in advanced ceramics (e.g., silicon carbide, aluminum oxide, boron carbide) under dynamic loading conditions. Key results of that study were[55] that changes to the apparent Poisson's ratio were more indicative of damage than changes to Young's modulus, and that both forms of mechanical damage were nonlinear and non-monotonic with respect to strain. The apparent Young's modulus was observed to increase above pristine quasi-static values just before failure in many of the tests, which stands in contrast to prior models that assume that physical damage can only manifest as a decrease in apparent Young's modulus[47,57–59]. Based on prior models[45,47,48] and experiments[32,54,60], this apparent increase in Young's modulus was hypothesized to be caused by the closure of pre-existing cracks with crack faces normal to the loading direction. Crack-closure explains the apparent increase in stiffness by requiring a reduction in apparent Poisson's ratio due to material moving axially into the void space instead of expanding laterally outward. This pore-collapse-type behavior has been seen in *in situ* scans of concrete under triaxial compression[60] and in scanning electron microscope images of rocks under uniaxial compression[6]. From scanning electron microscopy and X-ray tomography by Lo *et al.* [56], Li *et al*.[61], and Amirian *et al*.[62], the scale of these voids in pristine materials are on the order of micrometers, reducing the extent to which crack closure behavior can manifest before material failure.

Building on these past works to understand both how physical damage arises and evolves in brittle materials and how mechanical damage manifests in brittle materials under various loading conditions, this paper explores the effects of physical damage on mechanical damage evolution. This paper uses thermal shock to induce internal cracking in samples as described by Lo *et al*.[63] and extends the use of mechanical damage analysis[55] to these already damaged materials. By introducing large internal cracks without fully fragmenting the material before loading, the crack closure phenomenon seen in non-ceramic brittle materials[6,32,46,49,52–54,60,64] can be studied within the context of advanced ceramics under uniaxial compression. In

addition, this study also explores the use of the shear modulus change as a method of explaining observed mechanical damage accumulation, as compressive loads need to be translated into local tensile[65–68] or shear loading[16–18,48,69–71] in order to result in physical damage. This paper thus investigates the complexities of damage accumulation under uniaxial compression, and using analytic methods in order to present how physical damage relates to the evolution of apparent mechanical damage evolution.

2. Experimental Setup & Methods

a. Experimental Set Up

Material behaviors in this investigation are studied within a context of uniaxial compression, using samples machined into cuboids of dimensions of 3.5 mm x 2.7 mm x 2.3 mm. These sample sizes were used in both quasi-static and dynamic testing and were chosen to conform with prior samples[20], but reduced in dimensions in order to produce higher pressures with less force used, particularly in Kolsky bar experiments. The material of interest in this study was AD995 alumina from CoorsTek, Inc., with the "995" portion of the name referring to the fact that the material is 99.5% aluminum oxide by mass, with the remaining 0.5% being silicon dioxide. AD995 was selected for use because of its ease of acquisition and for being a representative material used in armor and industry[36,40,71–74]. Additionally, it has been used in previous papers by the authors of this study[55,75], providing a commonality of data. The previously gathered data[75] showed that AD995 had average grain sizes of 8.0 ± 3.0 μm, minimal internal void spaces, and the silica is located at the grain boundaries as part of the interstitial material rather than present as large defects or incorporated into the grains. AD995 is, thus, almost entirely homogenous, and the only source of difference in material properties from another alumina of equal chemical purity would be from grain sizes. Temperatures of 1300°C are considered 'low' for sintering high purity alumina[76] and, thus, keeping the thermal shock temperature well below this level means that the only microstructural changes will come from the thermal shock, and not grain growth or recrystallization. Where materials such as boron carbide have graphitic inclusions[20] and additives can produce complex phase structures[11,39,77–79], AD995 is not known to have any of these complexities.

To produce internal cracks and damage in the alumina, the ceramic samples were thermally shocked in preparation for testing by heating them with a butane torch for 120 seconds and then

visually checking for uniform thermal glow, and heating for an additional 30 seconds if glow was not uniform and repeating the inspection. By this method the samples were heated until above 750 °C. Thermal shock is then achieved by quenching the sample in room temperature water, causing the exterior of the sample to rapidly drop. This rapid temperature change is capable of causing the formation of internal cracks that have been shown to lead to mechanical damage in ceramics[80]. Previous studies focusing on the behavior of pre-damaged materials have primarily been interested in geomaterials[50,52–54] or concrete[32,60] damaged by mechanical forces. Testing of pre-damaged advanced ceramics has usually been limited to repeated loadings under dynamic conditions[81,82] or studying already comminuted powders[83], but Krimsky *et al.*[84] have used thermal shocking on boron carbide. In Krimsky *et al.*[84], the pre-damaged samples were subjected to one or two cycles of heating and quenching, and then characterized with X-ray computed tomography to determine crack surface area. The thermal shock method is preferred for this study because the degree of damage can be controlled by subjecting the samples to repeated heating and shocking cycles, with each sample in this study being subjected to between 1 and 8 cycles to produce a variety of damaged states. If a sample exhibited external physical damage such as surface delamination or loss of integrity, it was excluded from further testing. X-ray computed tomography was used by *Lo et al.* [56] to confirm the presence of internal cracks, with Figure 1 showing reconstructions of these internal cracks for three samples subjected to one, two, and eight thermal shock cycles. From Figure 1 it can be seen that one shock cycle produces physical damage, and eight shock cycles produces significantly more physical damage than one cycle. The difference between one and two shock cycles is, however, not as great as between zero and one or one and eight cycles, and thus the number of shock cycles should be taken as a qualitative measure of physical damage. As a result of the complexity of crack size, orientation, and their interactions with respect to loading direction, the number of shock cycles and the amount of physical damage present remains a qualitative measure for this study. Information on the number of cycles applied to each sample and the resulting peak compressive failure stress and failure strains found during testing are shown in Table 1. Samples are labelled according to the number of shock cycles (SC) they went through, whether they were subjected to quasi-static (QS) or dynamic (DYN) loading, and what sequence in a series of similar conditions they were subjected to. For example, SC0QS01 is the first quasi-static sample subjected to no shock cycles (i.e. pristine), while SC4DYN02 is the

second dynamic sample subjected to four shock cycles. The mechanical response of pristine dynamic samples have been previously described in Koch *et al.*[55], and four quasi-static pristine tests are included in this study for completeness. In addition, a quasi-static baseline derived from manufacturer specifications is included in many of the figures demonstrating mechanical property measurements, and this serves to show the behavior that would be expected in a purely brittle elastic response.

In these studies, the quasi-static compressive strength and Young's modulus were independently examined using an MTS 810 materials testing machine that compressed samples to failure. The servo-hydraulic controls allowed for precise measurement of forces, and Digital Image Correlation (DIC) was used to determine axial and lateral strains. The DIC setup is discussed in a subsequent paragraph. A Promon U750 camera recording at 100 Hz were used to capture the entirety of a 30 to 50-second-long quasi-static experiment. While the framerate was sufficient to capture axial and lateral strain data that could be used to calculate Young's modulus and Poisson's ratio values, 100 Hz is insufficient to capture the behavior of samples during actual failure (i.e. post-peak stress), as the events occur too quickly. For pristine samples, this yields no additional data beyond verification of manufacturer values. These mechanical values are a Young's modulus of 370 GPa, a Poisson's ratio of 0.22, and a failure strength of 2.70 GPa[85]. The quasi-static values of Young's modulus and Poisson's ratio are used as the pristine values when determining damage later. For the damaged samples subjected to quasi-static testing, their stress-strain and lateral vs. axial responses are non-linear and of interest to this study in seeking to understand relationships between physical (pre-cracking) and mechanical damage (Young's modulus and Poisson's ratio evolution).

Dynamic testing was done using a Kolsky bar testing apparatus and an ultra-high-speed Shimadzu HPV-X2 camera capable of capturing at ten million frames per second and 400 x 250 pixel resolution. For the experiments performed here, a framerate of 500,000 to 2,000,000 frames per second (FPS) was used at full resolution, and the camera system was coupled with a K2 Infinity Lens to fill the sample in the 4 mm by 6.5 mm field of view of the camera, with an example of such an image seen in Figure 2. The Kolsky bar apparatus used incident and transmitted bars that were 12.7 mm in diameter and made of maraging steel (Service Steel America C-350) with a Young's modulus of 200 GPa, Poisson's ratio of 0.29, yield strength of

2.68 GPa, and a density of 8100 kg/m^3. The incident bar was 101.6 cm in length, while the transmitted bar was 91.4 cm in length. Using compressed gas to provide the impulse, a projectile made from maraging steel was launched into an incident bar, which produces a strain pulse from the impact. The strain pulse is the transmitted into a ceramic sample held between the incident and transmission bars. The strain signal received by the transmission bar corresponds to the strain received by the sample while it was intact and remained in contact with both bars. In order to protect the incident and transmission bars from damage by the harder ceramic samples, 5 mm thick and 7.94 mm diameter tungsten carbide platens jacketed in 12.7 mm outer diameter titanium rings were used. High pressure grease was applied at the platen-sample interfaces in order to reduce the transmission of lateral or shear strains from the bars into the samples and to ensure that the input pulse was as uniaxial as possible. This setup is consistent with others in the literature, as noted by round robin testing performed under the supervision of Swab and Quinn[86]. A near-triangular pulse is considered ideal in Kolsky bar experiments for brittle materials[64,87], and this was achieved by using a 3.175 mm diameter and 1 mm thick tin pulse shaper, with a final strain rate on the order of 10^1 to 10^2 s^{-1} occurring over a pulse length of 200 μs. These pulse durations are much longer than typically used in the literature of 50 to 100 μs rise times[64,87], but have allowed us to achieve good stress equilibrium[55] and measurements[56] for the purpose of our current study. As a demonstration of equilibrium in the experiments in this paper, **Error! Reference source not found.** shows axial strain vs. time and stress vs. time simultaneously for SC0DYN02. Axial strains are shown for both the entire area of interest and for sub-sections of the sample surface (right in Figure 3), which shows that the strain field is uniform and the stress follows the strain, showing uniform deformation and good equilibrium. This methodology has previously been described and validated by Lo *et al.*[63] and Koch *et al.*[55]. In the experiments, strain was measured by six strain gauges arranged in three pairs, with two pairs on the incident bar, and one pair on the transmitted bar. Each pair had an additional two gauges not connected to the bars but connected together to form a full wheatstone bridge, with each bridge connected to its own Vishay 2310b amplifier, which sent their signals to an HBM Gen3i high speed portable data acquisition system sampling at 2 million samples per second. The strain gauge types were Micro-Measurements CEA-06-250UN-350 350 ohm resistance gauges secured in place via cyanoacrylate adhesive. Tests were only considered successful when strain responses and camera images confirmed that samples failed in loading on

the first loading pulse through the material. This setup has been used previously in Koch *et al.* [75]and Lo *et al.*[88] and has been established as part of the state-of-the-art in ceramics Kolsky bar round robin supervised testing by Swab and Quinn[86].

Digital image correlation techniques were applied to camera images from the quasi-static and dynamic tests in order to obtain lateral and axial strain measurements of the samples. DIC is a computer vision method used to track changes in the position of speckle patterns on the surface of an object in order to compute deformation fields, and has been well established in the study of many different materials[65,89–92]. DIC has been used previously in Kolsky bar experiments by the authors [55,61–63,88]. Due to the small size of the samples in our study, special measures were required to produce a speckle pattern that would produce more accurate measurements and lower error in correlation, requiring use of an airbrush with a 0.15 mm nozzle in order to produce speckles (speckles are seen in Figure 2) which corresponds to speckle areas of approximately 1300 to 2600 μm^2. Due to the high speed of image capture and thus low exposure times (~200 ns), a high gloss metallic paint for the speckles and high intensity LED ring light (REL Inc.) were required in this study to produce sufficient contrast in the images. DIC analysis was done using the commercial VIC-2D (v6 2018) software from Correlated Solutions (Irmo, South Carolina, USA), with the regions of interest discretized into 27 by 27 pixel subsets with a step size of 7 pixels. Correlation analysis was carried out using the optimized 8-tap interpolation scheme, with the shape function being internal to the software but based on derivatives of displacements and using a zero-normalized sum of squared differences criterion. Pre-filtering of images was done with a low-pass filter, while subset weighting was done via a Gaussian weighting, with no additional post-processing smoothing. Overall confidence intervals for correlations were consistently within the range of 10^{-3} to 10^{-4} pixels, leading to measurement uncertainty arising primarily from equipment and taken to be no greater than a conservatively large 5% in total. The largest possible source of uncertainty was the initial size of the samples in the visual field, taken as being 0.1 mm out of the 2.7 mm side length of the 2.7 mm by 3.5 mm face used for measurement, which amounts to ~4% uncertainty. Strains were computed from the displacement fields using the engineering strain tensor in the DIC software. The computed strain histories were matched to the stress histories produced by strain gauges on the Kolsky bar to determine stress-strain curves for each of the experiments, as is commonly done in Kolsky bar experiments in the literature[64,93,94]. This produces stress-strain plots that do not need to assume material properties of the sample. As a result of stiffness not being assumed as constant and axial and lateral strains being independently measured, variations in the Young's modulus

and Poisson's ratio response can be tracked with time and strain, allowing us to track mechanical damage evolution in these properties.

b. Damage Quantification

With the experimental capacity to determine axial and lateral strain and stress all independently from each other, it becomes possible to measure apparent elastic properties such as Young's modulus and Poisson's ratio, and to examine how these properties deviate from linearity during loading. This study is focused on the deviation from linear elastic behavior, so normalizing the values against pristine values better illustrates change than simply plotting the apparent elastic response values. This normalization process also allows simpler comparisons between materials with different intrinsic properties, and the normalization produces values that can be compared to those predicted from previous models on damage accumulation in brittle materials[47,49,95]. With access to both Young's modulus and Poisson's ratio from the measurements of stress, and axial and lateral strain, Young's modulus and Poisson's ratio can each have their own damage term that accounts for how these properties evolve during loading, and these values can vary independently of one another mathematically. The values of Young's modulus and Poisson's ratio are not independent from each other in a physical sense, as the mechanical damage arises from physical phenomena that affect both properties simultaneously. It is through the interaction of mechanical damage for Young's modulus and Poisson's ratio that a more complete understanding of the underlying physical damage evolution can be determined. A more detailed derivation of the calculation of damage values is found in Koch *et al.*[55], where the important mechanical damage terms to the Young's modulus and Poisson's ratio being denoted as D_E and D_ν, respectively. From experiments performed in this paper, these values are calculated using Equations (1) and (2):

$$D_E = \frac{E_{app}}{E_0} - 1 \tag{1}$$

$$D_\nu = \frac{\nu_{app}}{\nu_0} - 1 \tag{2}$$

where E_0 and ν_0 are the pristine Young's modulus and Poisson's ratios determined from the quasi-static experiments, respectively, and E_{app} and ν_{app} are the apparent Young's modulus and

Poisson's ratio at each data point in a given experiment, respectively. The apparent elastic properties are calculated using Equations (3) and (4):

$$E_{app} = \frac{\sigma_{inst}}{\varepsilon_{x_{inst}}} \tag{3}$$

$$\nu_{app} = \frac{\varepsilon_{y_{inst}}}{\varepsilon_{x_{inst}}} \tag{4}$$

where σ_{inst} is the instantaneous stress, $\varepsilon_{x_{inst}}$ is the instantaneous axial strain, and $\varepsilon_{y_{inst}}$ is the instantaneous lateral strain, with "instantaneous" here referring to each individual stress-strain or lateral-axial strain data point collected for a given experiment. For these experiments, each DIC image paired with time-matched load data from the strain gauges represents a three-component data point that allows for E_{app} and ν_{app} to be calculated for a given strain, which can then be used to calculate D_E and D_ν for a given strain or time. In the discussion of the results probing the response of the undamaged and pre-damaged samples, the primary interest will be in damage accumulation with axial strain.

Investigating damage in the form of Equations (1) and (2) is also motivated by experimental data[55,61,88] where both D_E and D_ν varying simultaneously suggest phenomena such as crack closure that are not apparent when only analyzing one damage value at a time. Fortunately, there are elastic moduli that combine together Young's modulus and Poisson's ratio in their description, such as the shear and bulk modulus; tracking these are also of interest here to explain observed phenomena. For an isotropic linear elastic material, the shear modulus (*G*) is calculated from Young's modulus and Poisson's ratio by:

$$G = \frac{E}{2(1+\nu)} \tag{5}$$

The same process used by Koch *et al.*[55] to generate Equations (1) and (2) are used here to generate Equation (6), which gives the apparent shear modulus G_{app}:

$$G_{app} = \frac{E_{app}}{2(1+\nu_{app})} \tag{6}$$

with the apparent shear modulus calculated by the apparent E_{app} and ν_{app} produced by Equations (3) and (4), and the pristine shear modulus G_0 calculated through the insertion of the values of E_0 and ν_0 into Equation (5). With G_0 and G_{app} so calculated, the shear damage D_G can be calculated using Equation (7):

$$D_G = \frac{G_{app}}{G_0} - 1 \tag{7}$$

In these equations, D_E and D_ν are calculated from a single apparent elastic modulus each and are thus considered primary damage responses, while D_G is determined from two apparent elastic moduli and is, thus, viewed as a secondary damage measure. The calculation of D_G from Equation (7) serves as a complement to understanding D_E and D_ν together. Next, experimental results are discussed in three stages: direct experimental results, primary damage response, and secondary damage response. Each stage serves to expand upon the insights of prior stages to better understand how intact and physically damaged advanced ceramics behave during mechanical loading.

3. Results

a. Mechanical Properties

The stress-strain data curves for the twenty tests examined are seen in Figure 4, with the sample names described in Table 1. The legend in the figure denotes that the color of the curves are associated with the level of shock cycles (e.g., SC1 being 1 shock cycle), with repeated experiments denoted at the end of the label as 01, 02, etc. In Figure 4(a), the curves are plotted for all experiments and all levels of damage. In Figure 4(b) to 3(d), the stress-strain curves are sub-divided according to levels of damage and this helps with visualization when specific tests are discussed here. In all sub-figures, a straight red line is included to denote the mean quasi-static behavior of the alumina AD995 material, which serves as a reference for understanding the effect of damage on the stress-strain responses for both quasi-static and dynamic conditions. For the experiments on the intact (undamaged) samples, the average strength for the quasi-static tests

are 2.5±0.2 GPa and for the dynamic experiments are 3.9±0.1 GPa. The stiffness is 360±10 GPa for both, and the failure strain is 0.0068±0.004 for quasi-static and 0.0102±0.0002 for dynamic experiments. From Figure 4, the trend for the pre-damaged samples typically begin with an apparent Young's modulus 10-20% below pristine (290-325 GPa). The stress-strain curves then inflect after a certain level of axial strain, with the axial strain required for inflection generally being between 0.001 and 0.004 strain. The samples subjected to the most shock cycles have the highest inflection strains, but more shock cycles do not translate into a larger strain at the inflection point. The quasi-static tests all fail catastrophically at peak stress and no strain information is collected for post-peak collapse due to framerate and triggering challenges for the camera for quasi-static testing. In the dynamic samples, some post-peak strain behavior is captured, which forms discussions later. Generally, from Figure 4, the failure strains increase as they become more pre-damaged. For the pre-damaged dynamic experiments, the peak strength of the damaged samples is reduced to 3.0±0.4 GPa, and also generally decreases as a function of pre-damage. For the quasi-static experiments, the pre-damaged tests mostly have lower strengths than the intact tests, with exception to SC8QS01. Unfortunately, beyond 8 shock cycles, the specimen macroscale integrity becomes unstable, and the samples cannot be reliably handled before suffering external damage that renders them unsuitable for testing, and so we were unable to investigate higher shock cycle trends with the thermal shock approach. In the quasi-static tests, trends in strength as a function of pre-damage are complicated as the failure strength appears to increase as a function of shock cycles for quasi-static loading, which is, perhaps, counter-intuitive. This will be discussed later in the Discussion section. Lastly, noticeable are some interesting behaviors in Figure 4: 1. sample SC3DYN02 has a steeper stress-strain slope, which indicates a higher Young's modulus, and additionally SC3DYN02 has a lower failure strain than all other samples; and, 2. samples SC8DYN01 and SC8QS01 show a convergence of behavior near failure. Both show an increase in failure strain over pristine samples and both have high inflection points, with SC8DYN01 inflecting at 0.0033 strain and SC8QS01 inflecting at 0.0051 strain. These samples were motivators for investigating damage accumulation in the shear modulus as it will be shown later in the Discussion Section to provide an explanation for the behavior observed in these and other tests.

Next, we show the corresponding lateral vs. axial strain relationships for all intact and pre-damaged tests in Figure 5. Again, the figure is sub-divided based on pre-damage levels for improved visualization and a legend is included where color notes the level of shock. The baseline quasi-static behavior (red line) is also shown in each sub-figure for reference on the effect of damage on the lateral vs. axial strain relationships. Note the y limits for sub-figures (b) to (d) are magnified from (a) in order to show more distinct trends, with asymptotic behavior for each experiment still clear in (a). For the intact experiments, the slope (or Poisson's ratio) of the lateral vs. axial strain is 0.22±0.01 for the quasi-static experiments and 0.29±0.08 for the dynamic experiments, and this is consistent with the manufacture's value of 0.22. For all pre-damaged samples across both rates in Figure 5, there is a region of non-increasing lateral strain for increasing axial strain at lower axial strains, followed by a mostly linearly increasing region for lateral strain as a function of axial strain. The inflection point does not strongly associate with the number of shock cycles. The non-increasing region is likely related to void collapse and crack closure, which will be discussed later in the Discussion Section. The rate of increase for lateral vs. axial strain behaviors of curves do not follow any clear trends in this plotting convention as a function of pre-damage or strain rate, nor do the inflection points. Trends become more apparent later when investigating these behaviors with respect to changes in shear modulus in Figure 9 and Figure 10. Dynamic tests generally show a larger lateral response than quasi-static tests of the same pre-damage level, with the exception of SC1QS01 having a greater lateral response than SC1DYN01 or SC1DYN02. The number of shock cycles does not seem to follow a significant trend in terms of average lateral strain at failure, with SC0 > SC4 > SC3 > SC1 > SC8 > SC2. The greatest lateral response tends to come during unloading for dynamic tests, but SC1QS01 demonstrates a series of abrupt jumps in lateral response during loading. These large lateral responses during unloading imply that internal cracks are growing internally and require additional volume to accommodate their growth and thus must expand laterally to do so. This unloading behavior is most extreme in SC0DYN01, where during unloading the strains measured by DIC become out of sync with the stresses measured by the strain gauges. This is seen in Figure 4 as the stress remaining near constant while the strain rapidly decreases. While non-physical in nature, what this result tells us is that the lateral expansion of the cracks is causing out-of-plane movement that the DIC is interpreting in part as a decrease in axial strain. This is supported by SC0DYN01 showing extreme lateral strain increase in Figure 5. The

equilibrium seen in Figure 3 and the pristine quasi-static values conforming to manufacturer specifications indicate that our methodology is accurate up to failure (near peak stress). After failure the measurements are considered qualitative, as such post-peak behaviors are not well known in the literature for advanced ceramics due to the short time span (>10μs) they occur over.

The data taken from experiments to this point show a number of trends with physical damage (e.g., failure strain increasing with number of shock cycles), but also a number of anomalous behaviors (e.g., failure strength increasing with the number of shock cycles for quasi-static loading). The primary inferences that can be drawn from Figure 4 and Figure 5 on their own is that the relationship between physical damage and mechanical response is non-linear and non-monotonic. This is known to occur in geomaterials[52–54], but in those studies the degree of physical pre-damage was not as controlled. Further analysis of the material requires shifting from examining the stress-strain and lateral vs. axial curves to examining the primary mechanical damage values of D_E and D_ν. The most interesting features of these tests are associated with low stress-strain or lateral-axial responses that are not clearly observed in Figure 4 and Figure 5.

b. Damage Accumulation

The primary damage variables D_E and D_ν are calculated from the stress σ_{inst}, axial strain $\varepsilon_{x_{inst}}$, and lateral strain $\varepsilon_{y_{inst}}$, using Equations (3) and (4), respectively. The plotting of D_E vs. axial strain is shown in

Figure 6, and the plot of D_v vs. axial strain is shown in Figure 7. The same legend and sub-plotting scheme from Figure 4 and Figure 5 are used in

Figure *6* and Figure 7. The red line corresponding to the expected quasi-static behavior is also shown in both

Figure *6* and Figure 7, and this manifests as a horizontal line due to the fact that a purely linear elastic brittle response would demonstrate no damage of any sort up to failure. The samples in

Figure 6 all show large negative D_E values at lower strains before an inflection occurs, and the values begin to converge towards D_E = 0, with two exceptions. The first exception is SC0DYN01, which exhibits the opposite initial behavior by exceeding the pristine Young's modulus at low axial strains, before converging to D_E = 0, and then having an increasing D_E value during unloading. The second exception to the general trend is SC3DYN02, which passes its pristine stiffness and continues to increase its apparent Young's modulus up to failure, exceeding $D_E = 0$ and having $D_E = 0.30$ at failure. In isolation, this D_E behavior is hard to reconcile with past theory which suggests that brittle materials in compression should only lose stiffness with axial strain once crack growth begins[45,47,59]. Additional insights are found via examination of D_ν and D_G in Figure 7 and Figure 10, respectively.

Next, Figure 7 shows D_ν vs. axial strain, and reinforces the observations from Figure 5 in that damage does not accumulate in a consistent manner across all of the pre-damaged samples. Most of the pre-damaged samples show initial D_ν values of -0.5 or lower, and then these increase in D_ν as axial strain increases. The result of D_ν being positive at failure for the majority of the samples is the most important observation that can be drawn from these experimental observations. A positive D_ν involves the introduction of new volume to the system in order to increase Poisson's ratio above pristine, which is consistent with materials experiencing crack growth. The general description of the D_ν vs. axial strain is that the samples start with a negative D_ν, reach an inflection point, and then trend upwards. This trend of D_ν increasing before failure holds for all but SC1DYN01, as might be expected from crack closure[6,60]. However, they do not follow a consistent pattern for the number of shock cycles influencing the axial strain at which inflection occurs. The SC3DYN01, SC3DYN02, and SC4DYN01 samples that demonstrate unloading behavior with axial strain decrease also show a D_ν>1.5 at failure. Samples such as SC3DYN02 and SC4DYN01 have extreme values of D_ν at failure, being 7.6 and 12.7, respectively, which are not plotted with the other D_ν damage curves as they are so large as to obscure the primary behaviors between $-1 < D_\nu < 1$. These extreme values of D_ν are likely non-physical, but they do demonstrate how the large the lateral strains become in comparison to the axial strains, which provides information on what must be happening internally to produce such results. Additionally, all samples except SC1DYN01 demonstrate a positive D_ν at failure, indicating that their apparent Poisson's ratio has increased above the pristine quasi-static value of 0.22±0.01, which is a process that requires the introduction of new volume to the samples. Next, only SC8DYN01 has a strong inflection point in D_ν at the same strain as the strong inflection point in D_E, which is suggestive of extensive physical damage as this strong inflection suggests a change in physical processes involved in mechanical response. This observation coincides with knowledge that it has been subjected to the most thermal shock cycles of all samples and thus it is expected that it has the most physical damage. Finally, while only SC8DYN01 has a strong inflection point, its quasi-static counterpart of SC8QS01 also shows a transition from one form of behavior to another, with the mechanical damage at high axial strain following the same curve as the dynamic test with the same number of shock cycles. This convergence of behavior suggests a possible convergence of mechanical behavior between quasi-static and dynamic tests when the initial physical damage is large. However, with no

general trends emerging for D_v as a function of the number of shock cycles, further analysis of secondary damage measures such as D_G will be explored in Figure 8.

To now, the raw data and the primary damage values D_E and D_v have demonstrated some clear trends such as initial physical pre-damage producing initial D_E values below zero or failure being associated with $D_v > 0$, but outliers remain. It is at this point we move into the secondary damage values, and examine how D_G values calculated from Equation (7) influence understanding of the experiments. This understanding is first presented in Figure 8 for SC3DYN02 in specific and then explored for all cases in Figure 10. Previously, the greatest outlier of all of the pre-cracked materials examined in this study is SC3DYN02, as this sample shows a large increase in Young's modulus over pristine values and the lowest failure strain of all dynamic and quasi-static tests. By plotting D_E, D_v, D_G, and stress vs. axial strain in Figure 8 the anomalous behavior shows a clearer trend. Namely, D_G is negative or approximately zero through the entire loading process. When D_E becomes positive at 0.0041 axial strain then D_v has a sudden increase that causes D_G to become negative once again, undergoing a rapid decrease up to failure. As seen in

Figure 6, for most samples, D_E trends towards $D_E = 0$ as axial strain increases up to failure, while Figure 7 has D_ν demonstrating much more varied and asymptotic behavior before failure for all samples. Figure 8 also illustrates that when SC3DYN02 is plotted as D_G vs. axial strain, three loading phases are seen. The first phase, from 0 to 0.0041 axial strain has the sample starting with a low D_G value, with D_ν being negative and D_E being less than D_G. In the second phase from 0.0041 to 0.0049 axial strain, $D_G = 0 \pm 0.05$, indicating that the sample has an essentially pristine shear modulus even while D_E and D_ν are continuing to evolve. In the third phase, from 0.0049 strain to catastrophic fracture at 0.0057 axial strain in Figure 8, D_G rapidly decreases. This and evidence from other tests not shown for brevity suggests there are three distinct loading processes associated with D_G, which we propose to name *recovery*, *plateau*, and *failure stages*. Figure 9 shows D_G vs. axial strain curves for SC0DYN02, SC1DYN01, and SC4DYN01, with these stages highlighted to better show these changes in behavior. Notably, while SC0DYN02 and SC4DYN01 show distinct *failure stages*, SC1DYN01 does not show a *failure stage*, as the sample undergoes fragmentation that prevents DIC measurement of strains during unloading.

However, while SC1DYN01 has a lower D_G during the *plateau stage* than either SC0DYN02 or SC4DYN01 and has no *failure stage*, its *plateau stage* ends at the same strain as SC0DYN02 and at a higher strain than SC4DYN01. For these three tests the number of shock cycles does have an apparent correlation with a parameter, in that the length of the *plateau* increases with increasing pre-damage, and the length of the *recovery stage* decreases with increasing pre-damage. With these observations we can now examine all of the D_G vs. axial strain curves to demonstrate the patterns seen in Figure 8 and Figure 9 continue to hold.

Figure 10 shows D_G vs. axial strain for all pristine and pre-damaged samples, following the same conventions for panels (a) through (d) as in prior figures. Here it can be seen that all samples fail with a negative D_G value. For the pristine dynamic tests D_G values at ultimate failure are between -0.7 and -1.0, with -1.0 being a total loss of shear modulus, while the pre-damaged samples show D_G values at failure between -0.2 and -0.6. While it seems counter-intuitive for pristine samples to have greater D_G damage at ultimate failure than pre-damaged material, the overall curves help explain why pristine samples would have a more negative D_G value at ultimate failure. Namely, the more pre-damaged samples frequently have no *failure stage*, in comparison to the extended *failure stages* of the pristine samples. This lack of a *failure stage* is due to the fact that the samples fail catastrophically in a way that DIC cannot capture the change in mechanical behavior while the material physically disintegrates. For example, in Figure 10 the pristine SC0DYNX samples, SC3DYN01, SC3DYN02, SC4DYN01, and SC3DYN03 demonstrate definite *failure* sections. Specifically, SC1QS01 demonstrates large drops in D_G during loading, caused by the large jumps in lateral vs. axial strain seen in Figure 5(a) at 0.0030 and 0.0064 strain. All other pre-damaged samples have their curves end with no distinct *failure stage*. This suggests that intact materials are able to tolerate a *failure stage* before fracturing, while the samples with more pre-damage will fracture as soon as the *failure stage* begins. Further examination of the tests in Figure 10(c) shows how physical damage increases could change how mechanical damage behavior manifests. Figure 10(c) contains the samples that underwent 1, 2, or 3 shock cycles and, thus, there is an increasing amount of pre-damage. Here the SC1 series demonstrate the lowest D_G *plateau* values of the three shock cycle series shown, no distinct *failure stage*, and low failure strain. The SC2DYN01 test shows the highest failure strain, and during the *plateau stage*, demonstrates a D_G value between that of the SC1 and SC3 samples. Finally, the SC3DYN01 and SC3DYN02 show the greatest recovery of shear modulus, but also considerably lower failure strains and pronounced *failure stages*. Comparing between quasi-static tests alone, SC1QS01 has a much lower D_G and failure strain at fracture (D_G = -0.64 at 0.0076 strain) than SC3QS01 (D_G = -0.15 at 0.0084 strain). This suggests that physical damage manifests as mechanical damage in a complex manner that affects the ability of the sample to tolerate shear modulus degradation. Combining the general observations of Figure 10 with the insights from Figure 9, a trend emerges: samples with a low number of shock cycles exhibit large initial degradations in the shear modulus and are prone to fragmentation without a distinct *failure stage*, but their

plateau stages reach approximately the same axial strain as the pristine materials. As the amount of pre-damage increases, the materials have higher initial D_G values and greater recovery towards $D_G = 0$, but at the cost of the *failure stage* beginning at lower axial strains. The presence of *failure stages* in highly pre-cracked material thus becomes indicative of early failure. SC8DYN01 reverses this trend by having a low value of D_G initially and at failure, and by having the highest failure strain of all tests, but the behavior of SC8DYN01 is convergent with SC8QS01. These and other previously noted behaviors are further examined in the Discussion in the context of the relationship between physical damage and mechanical damage.

4. Discussion

This research has discovered a number of key points about the relationship between physical damage and mechanical damage, and how the accumulation of both serves to degrade properties, which are summarized as:

1.) Physical damage reduces mechanical properties such as failure strength, failure strain, and apparent Young's modulus, but it is not a linear relationship where more physical damage results in more mechanical damage as previously assumed [34,47,59,95,96], and there is an additional interaction when comparing dynamic to quasi-static loading;

2.) Quantitative end points such as failure stress and strain are insufficient to explain the behavior of pre-damaged material, as the accumulation of damage involves a series of stages from the *recovery stage* to the *plateau stage* to the *failure stage*, each with different behaviors that depend on initial and current physical damaged states; and

3.) Damage to the shear modulus (D_G) of a material appears to be the most indicative factor for damage accumulation as a criterion for failure rather than damage to Young's modulus (D_E) or Poisson's ratio (D_ν). All of these points have not been predicted by prior models of brittle fracture processes[34,47,59,95,96], but elements of the physical phenomenon have been seen in other fields[6,46,48,50,52–54,97] that will guide the interpretation of the observations made in this paper.

First, the complex relationship between physical damage, mechanical damage, their evolution, and strain rate is well illustrated in Table 1,

Figure 6, Figure 7, and Figure 10. The data there shows that the physical damage caused by thermal shock reduces failure strength, failure strain, and initial apparent Young's modulus, while dynamic loading increases failure strength and failure strain in comparison to quasi-static loading. However, increasing physical pre-damage causes quasi-static failure strength and failure strain to increase, even above the pristine value, which has profound implications for models that use the quasi-static failure strength as an input, such as the JH-2 model[34], the Paliwal-Ramesh[47], or Hu-Ramesh[59] models. This phenomenon of improved quasi-static performance and degraded dynamic performance has been observed in advanced ceramics in the past, with Arab *et al.*[97] showing that the addition of SrO_3 to zirconia toughened alumina was able to increase fracture toughness under quasi-static conditions with a specific percentage addition of SrO_3, but decreased fracture toughness under dynamic loading for all percentages. This was attributed to the SrO_3 forming a secondary phase at grain boundaries that increased the porosity of the material, which increased the fracture toughness in quasi-static loading when there was an optimal concentration of SrO_3, but weakened the material for dynamic loading in all cases. This exact behavior can be seen with SC8QS01 and SC8DYN01, with SC8QS01 showing greater failure strength and strain than pristine, which, on their own, suggest that the material has superior failure strength despite being the most highly damaged sample. SC8DYN01 on the other hand has the lowest D_G during its *plateau stage* of all the dynamic tests, and since the purpose of the thermal shocks is to produce internal cracking and thus increase the porosity of the material, the situation is analogous to what occurred with Arab *et al*.[97]. The complexity of how physical damage manifests in mechanical damage across multiple potential performance metrics, such as failure strength or apparent Young's modulus response, suggests that there are multiple possible mechanisms for the material to accommodate strain, and which mechanisms are dominant during a test depends upon the interaction of pre-damage, total strain experienced, and strain rate. The complex relationship between the responses feed into the second point about the importance of how damage accumulates with increasing strain, and this is explored next.

Following on the idea that the thermal shock induced physical damage has a complex effect on the mechanical response of the materials, it can be seen that the SC0DYN series have a noticeably different shape from the SC8 samples, even though by Table 1 a sample experiencing eight thermal shock cycles results in an average failure strength 77±5% of pristine and a 6±2% increase in failure strain. Qualitatively, the behavior seen in Figure 4, Figure 5,

Figure 6, Figure 7, and Figure 10 are distinct between the pristine, moderately damaged, and most damaged samples. Examining Figure 10 by seeking the *recovery*, *plateau*, and *failure stages*, the trend suggested is that the pre-cracking physical damage is something the material accommodates through the rearrangement of cracks at the cost of reducing the strain at which the *plateau stage* ends and thus the *failure stage* begins. At a low number of shock cycles, the amount of apparent rearrangement is low, as seen in Figure 9 by the way SC1DYN01 has a relatively short *recovery stage* and a change in D_G of 0.0060 between the start and end of the *plateau stage*. This rearrangement to accommodate stress reduces apparent shear modulus and reduces the capacity to sustain a *failure stage*. For SC4DYN01 in Figure 9, the initial loss of shear modulus is lower than the less damaged SC1DYN01, but its *plateau stage* ends at a lower strain than SC0DYN02 or SC1DYN01, and the other SC4DYN curves in Figure 10 shows that the early failure is even more pronounced in SC4DYN02 and SC4DYN03. Just within Figure 10(c), going from 1 shock cycle to 3 shock cycles shows an increased *recovery* of D_G, but the *failure stage* begins at lower strains and the more pre-damaged samples show larger changes in D_G than the less pre-damaged samples, which fracture at the end of their *plateaus*.

Second, extending and interpreting the second discussion point, the presence and absence of the *recovery* and *failure stages* allows for the complex interaction of pre-damage and strain rate effects to be better understood. Comparing SC0DYN to SC0QS shows that the dynamic tests have a recovery period where $D_G \neq 0$ while the quasi-static tests remain at $D_G = 0$, and for all samples with pre-damage up to the SC8 series, the dynamic tests have a higher failure strain than the quasi-static tests. One inference is that starting from pristine quasi-static as a baseline, pre-damage past the first shock cycle and dynamic loading have a similar effect: a recovery period and an increased failure strain. The first shock cycle is the exception, likely due to the difference

in pre-existing flaws between SC0 and SC1 being much larger than between SC1 and SC8, with any intermediate behaviors not captured. The fact that pre-damage and dynamic loading have similar mechanical responses suggests that a similar physical mechanism is responsible for both behaviors. This physical response is hypothesized here to be the activation of additional flaws, identified in the literature to be a cause of the difference in behavior between quasi-static and dynamic response[98]. In a sample with large amounts of initial pre-damage, the cracks have to be rearranged to support applied loads, forcing the activation of flaws smaller than the most significant flaw in order to facilitate load transfer to the bulk material. Under dynamic loading this is caused by the material not having sufficient time to communicate the presence of a loading event to the most significant flaw without activating other flaws in the way[98]. This similarity in response between pre-damage and dynamic loading suggests that the early *recovery* and *plateau stages* may contain important information on how a ceramic will perform once it reaches the *failure stage*.

The third discussion point to address is that the shear modulus shows a more useful description of the behaviors expected to arise from physical damage than the apparent Young's modulus or Poisson's ratio demonstrate. Prior findings[55] already suggested that the Poisson's ratio damage was more indicative of accumulating physical damage than Young's modulus damage for brittle materials subjected to dynamic loading, but this paper now shows that their combined behavior in the apparent shear modulus is more indicative. As seen in the behavior of SC3DYN02, the apparent Young's modulus can increase, so long as Poisson's ratio increases faster, and, thus, shear modulus decreases. This is a key insight for models that use a damage term, as those models assume that their equivalent terms for damage D_E vary from 0 to -1[34,47,59,95,96]. Taking Equations (5) through (7) and assuming that Poisson's ratio remains constant ($\nu_{app} = \nu_0$) produces Equation (8):

$$D_G = \frac{\frac{E_{app}}{2(1+\nu_0)}}{\frac{E_0}{2(1+\nu_0)}} - 1 = \frac{E_{app}}{E_0} - 1 = D_E \tag{8}$$

Equation (8) states that under the assumption that ν does not change with an applied load that $D_G = D_E$, which means that any prior model making this assumption of Poisson's ratio

invariance would not distinguish which of these two elastic moduli was changing. With a growing recognition in the literature that shear plays an important role in the failure of brittle materials[17,18,43,48,69,71,75,99–101], the finding of shear modulus loss as an important metric in the failure of ceramics provides evidence for future focus on the study of shear failure in ceramics and how shear modulus damage evolution affects performance.

5. Conclusion

In this paper, we have combined together thermal shocking of ceramics to induce pre-damage via internal fracturing with previously developed techniques for combining DIC with Kolsky bar and load frame tests to observe mechanical damage accumulation with strain. Through this experimental set up we have been able to discover the complex manner in which strain rate and pre-damage interact with each other, and how physical damage manifests in non-linear and non-monotonic ways. In particular, dynamic loading can be divided into *recovery*, *plateau*, and *failure stages* that provide more information and context than end point measures such as failure strength or failure strains. It has also been discovered that changes to the shear modulus is more indicative of physical damage accumulation during mechanical loading than changes to Young's modulus or Poisson's ratio.

Statement of Interests

Brendan M. L. Koch, Calvin Lo, and Haoyang Li are all students of James D. Hogan at the University of Alberta, and have no additional interests.

James D. Hogan is an associate professor at the University of Alberta, located in Edmonton, Alberta, Canada. He heads the research group the Center for Advanced Material Design (CDAM). He receives public funding from NSERC and private funding from industry and government collaborators.

Tomoko Sano and Jonathan Ligda are employees of the United State Army Research Laboratory.

This research was sponsored by the U.S. Army Research Laboratory and was accomplished under Cooperative Agreement Number W91NF-16-2-0079 and W911NF-17-2-0213. The views and conclusions contained in this document are those of the authors and should not be interpreted as representing the official policies, either expressed or implied, of the Army Research Laboratory or the U.S. Government. The U.S. Government is authorized to reproduce and distribute reprints for Government purposes notwithstanding any copyright notation herein.

Acknowledgements

This research was sponsored by the U.S. Army Research Laboratory and was accomplished under Cooperative Agreement Number W91NF-16-2-0079 and W911NF-17-2-0213. The views and conclusions contained in this document are those of the authors and should not be interpreted as representing the official policies, either expressed or implied, of the Army Research Laboratory or the U.S. Government. The U.S. Government is authorized to reproduce and distribute reprints for Government purposes notwithstanding any copyright notation herein.

References

[1] W.F. Brace, E.G. Bombolakis, A note on brittle crack growth in compression, J. Geophys. Res. 68 (1963) 3709–3713.

[2] W.B. Bradley, A.S. Kobayashi, An investigation of propagating cracks by dynamic photoelasticity, Exp. Mech. 10 (1970) 106–113.

[3] A. Chudnovsky, M. Kachanov, INTERACTION OF A CRACK WITH A FIELD OF MICROCRACKS, Lett. Appl. Eng. Sci. 21 (1983) 1009–1018.

[4] M.F. Ashby, S.D. Hallam, The Failure of Brittle Solids Containing Small Cracks Under Compressive Stress States, Acta Metall. 34 (1986) 497–510.

[5] B. Aydelotte, B. Schuster, Observation and Modeling of Cone Cracks in Ceramics, in: B. Song, L. Lamberson, D. Casem, J. Kimberley (Eds.), Dyn. Behav. Mater. Vol. 1, Springer International Publishing, Cham, 2016: pp. 19–23. http://link.springer.com/10.1007/978-3-319-22452-7_4 (accessed December 14, 2016).

[6] P.-Q. Ji, X.-P. Zhang, Q. Zhang, A new method to model the non-linear crack closure behavior of rocks under uniaxial compression, Int. J. Rock Mech. Min. Sci. 112 (2018) 171–183. https://doi.org/10.1016/j.ijrmms.2018.10.015.

[7] M. Chen, Shock-Induced Localized Amorphization in Boron Carbide, Science. 299 (2003) 1563–1566. https://doi.org/10.1126/science.1080819.

[8] W. Braue, B. Hildmann, H. Schneider, U. Hornemann, The crystalline-to-amorphous transition in shock-loaded mullite Al2VI(Al2+2xSi2−2x)IVO10−x in the light of shear modulus anisotropy, J. Eur. Ceram. Soc. 29 (2009) 3135–3146. https://doi.org/10.1016/j.jeurceramsoc.2009.05.051.

[9] D. Ghosh, G. Subhash, J.Q. Zheng, V. Halls, Influence of stress state and strain rate on structural amorphization in boron carbide, J. Appl. Phys. 111 (2012) 063523. https://doi.org/10.1063/1.3696971.

[10] G. Subhash, D. Ghosh, J. Blaber, J.Q. Zheng, V. Halls, K. Masters, Characterization of the 3-D amorphized zone beneath a Vickers indentation in boron carbide using Raman spectroscopy, Acta Mater. 61 (2013) 3888–3896. https://doi.org/10.1016/j.actamat.2013.03.028.

[11] A.P. Awasthi, G. Subhash, High-pressure deformation and amorphization in boron carbide, J. Appl. Phys. 125 (2019) 215901. https://doi.org/10.1063/1.5091795.

[12] Q. An, W.A. Goddard, K.Y. Xie, G. Sim, K.J. Hemker, T. Munhollon, M.F. Toksoy, R.A. Haber, Superstrength through Nanotwinning, Nano Lett. 16 (2016) 7573–7579. https://doi.org/10.1021/acs.nanolett.6b03414.

[13] X. Li, S. Yin, S.H. Oh, H. Gao, Hardening and toughening mechanisms in nanotwinned ceramics, Scr. Mater. 133 (2017) 105–112. https://doi.org/10.1016/j.scriptamat.2017.02.003.

[14] D.R. Curran, L. Seaman, T. Cooper, D.A. Shockey, Micromechanical model for comminution and granular flow of brittle material under high strain rate application to penetration of ceramic targets, Int. J. Impact Eng. 13 (1993) 53–83.

[15] M.W. Chen, J.W. McCauley, J.C. LaSalvia, K.J. Hemker, Microstructural Characterization of Commercial Hot-Pressed Boron Carbide Ceramics, J. Am. Ceram. Soc. 88 (2005) 1935–1942. https://doi.org/10.1111/j.1551-2916.2005.00346.x.

[16] Z.P. Bažant, F.C. Caner, Comminution of solids caused by kinetic energy of high shear strain rate, with implications for impact, shock, and shale fracturing, Proc. Natl. Acad. Sci. 110 (2013) 19291–19294.

[17] Z.P. Bažant, F.C. Caner, Impact comminution of solids due to local kinetic energy of high shear strain rate: I. Continuum theory and turbulence analogy, J. Mech. Phys. Solids. 64 (2014) 223–235. https://doi.org/10.1016/j.jmps.2013.11.008.

[18] Z.P. Bažant, Y. Su, Impact Comminution of Solids Due to Progressive Crack Growth Driven by Kinetic Energy of High-Rate Shear, J. Appl. Mech. 82 (2015) 031007. https://doi.org/10.1115/1.4029636.
[19] D.A. Shockey, A.H. Marchand, S.R. Skaggs, G.E. Cort, M.W. Burkett, R. Parker, Failure Phenomenology of Confined Ceramic Targets and Impacting Rods, Int. J. Impact Eng. 9 (1990) 263–275.
[20] J.D. Hogan, L. Farbaniec, M. Shaeffer, K.T. Ramesh, The Effects of Microstructure and Confinement on the Compressive Fragmentation of an Advanced Ceramic, J. Am. Ceram. Soc. 98 (2015) 902–912. https://doi.org/10.1111/jace.13353.
[21] J.D. Hogan, L. Farbaniec, N. Daphalapurkar, K.T. Ramesh, On Compressive Brittle Fragmentation, J. Am. Ceram. Soc. 99 (2016) 2159–2169. https://doi.org/10.1111/jace.14171.
[22] J.D. Hogan, L. Farbaniec, T. Sano, M. Shaeffer, K.T. Ramesh, The effects of defects on the uniaxial compressive strength and failure of an advanced ceramic, Acta Mater. 102 (2016) 263–272. https://doi.org/10.1016/j.actamat.2015.09.028.
[23] D.M. Collins, M. Mostafavi, R.I. Todd, T. Connolley, A.J. Wilkinson, A synchrotron X-ray diffraction study of in situ biaxial deformation, Acta Mater. 90 (2015) 46–58. https://doi.org/10.1016/j.actamat.2015.02.009.
[24] D.M. Collins, T. Erinosho, F.P.E. Dunne, R.I. Todd, T. Connolley, M. Mostafavi, H. Kupfer, A.J. Wilkinson, A synchrotron X-ray diffraction study of non-proportional strain-path effects, Acta Mater. 124 (2017) 290–304. https://doi.org/10.1016/j.actamat.2016.11.011.
[25] E.N. Landis, D.T. Keane, X-ray microtomography for fracture studies in cement-based materials, in: Dev. X-Ray Tomogr. II, International Society for Optics and Photonics, 1999: pp. 105–114.
[26] E. Maire, C. Le Bourlot, J. Adrien, A. Mortensen, R. Mokso, 20 Hz X-ray tomography during an in situ tensile test, Int. J. Fract. 200 (2016) 3–12. https://doi.org/10.1007/s10704-016-0077-y.
[27] E. Strassburger, High-Speed Photographic Study of Wave Propagation and Impact Damage in Transparent Aluminum Oxynitride (AION), DTIC Document, 2006. http://oai.dtic.mil/oai/oai?verb=getRecord&metadataPrefix=html&identifier=ADA457205 (accessed September 26, 2016).
[28] E. Strassburger, Stress wave and damage propagation in transparent laminates at elevated temperatures, DTIC Document, 2010. http://oai.dtic.mil/oai/oai?verb=getRecord&metadataPrefix=html&identifier=ADA519117 (accessed September 26, 2016).
[29] E. Strassburger, P. Patel, J.W. McCauley, C. Kovalchick, K.T. Ramesh, D.W. Templeton, High-speed transmission shadowgraphic and dynamic photoelasticity study of stress wave and impact damage propagation in transparent materials and laminates using the edge-on impact (EOI) method, DTIC Document, 2008. http://oai.dtic.mil/oai/oai?verb=getRecord&metadataPrefix=html&identifier=ADA479090 (accessed September 26, 2016).
[30] J.Y. Huang, J.C. E, J.W. Huang, T. Sun, K. Fezzaa, S.L. Xu, S.N. Luo, Dynamic deformation and fracture of single crystal silicon: Fracture modes, damage laws, and anisotropy, Acta Mater. 114 (2016) 136–145. https://doi.org/10.1016/j.actamat.2016.05.022.
[31] S. Bavdekar, G. Subhash, Comparison of pressure-sensitive strength models for ceramics under ultrahigh confinement, Int. J. Impact Eng. 118 (2018) 60–66. https://doi.org/10.1016/j.ijimpeng.2018.04.007.
[32] Y. Hao, H. Hao, G.P. Jiang, Y. Zhou, Experimental confirmation of some factors influencing dynamic concrete compressive strengths in high-speed impact tests, Cem. Concr. Res. 52 (2013) 63–70. https://doi.org/10.1016/j.cemconres.2013.05.008.
[33] M. Salviato, K. Kirane, Z.P. Bazˇant, Statistical distribution and size effect of residual strength of quasibrittle materials after a period of constant load, J. Mech. Phys. Solids. 64 (2014) 440–454. https://doi.org/10.1016/j.jmps.2013.12.005.

[34] G.R. Johnson, T.J. Holmquist, An improved computational constitutive model for brittle materials, in: AIP Conf. Proc., AIP, Colorado Springs, Colorado (USA), 1994: pp. 981–984. https://doi.org/10.1063/1.46199.
[35] B.J. Dalgleish, A. Fakhr, P.L. Pratt, R.D. Rawlings, The Fracture Toughness-Microstructure Relationship of Alumina-Based Ceramics, (n.d.) 2031–2038.
[36] M. Guazzato, M. Albakry, S.P. Ringer, M.V. Swain, Strength, fracture toughness and microstructure of a selection of all-ceramic materials. Part I. Pressable and alumina glass-infiltrated ceramics, Dent. Mater. 20 (2004) 441–448. https://doi.org/10.1016/j.dental.2003.05.003.
[37] A.D. Norton, S. Falco, N. Young, J. Severs, R.I. Todd, Microcantilever investigation of fracture toughness and subcritical crack growth on the scale of the microstructure in Al 2 O 3, J. Eur. Ceram. Soc. 35 (2015) 4521–4533. https://doi.org/10.1016/j.jeurceramsoc.2015.08.023.
[38] N.P. Padture, B.R. Lawn, Toughness Properties of a Silicon Carbide with an in Situ Induced Heterogeneous Grain Structure, J. Am. Ceram. Soc. 77 (1994) 2518–2522. https://doi.org/10.1111/j.1151-2916.1994.tb04637.x.
[39] N.A. Rejab, A.Z.A. Azhar, K.S. Kian, M.M. Ratnam, Z.A. Ahmad, Effects of MgO addition on the phase, mechanical properties, and microstructure of zirconia-toughened alumina added with CeO2 (ZTA–CeO2) ceramic composite, Mater. Sci. Eng. A. 595 (2014) 18–24. https://doi.org/10.1016/j.msea.2013.11.091.
[40] L.-S. Chang, T.-H. Chuang, W.J. Wei, Characterization of alumina ceramics by ultrasonic testing, Mater. Charact. 45 (2000) 221–226. https://doi.org/10.1016/S1044-5803(00)00081-4.
[41] R.S. Lima, S.E. Kruger, G. Lamouche, B.R. Marple, Elastic Modulus Measurements via Laser-Ultrasonic and Knoop Indentation Techniques in Thermally Sprayed Coatings, J. Therm. Spray Technol. 14 (2005) 52–60. https://doi.org/10.1361/10599630522701.
[42] B.R. Goodlet, C.J. Torbet, E.J. Biedermann, L.M. Jauriqui, J.C. Aldrin, T.M. Pollock, Forward models for extending the mechanical damage evaluation capability of resonant ultrasound spectroscopy, Ultrasonics. 77 (2017) 183–196. https://doi.org/10.1016/j.ultras.2017.02.002.
[43] K.K. Phani, Correlation between ultrasonic shear wave velocity and Poisson's ratio for isotropic porous materials, J. Mater. Sci. 43 (2008) 316–323. https://doi.org/10.1007/s10853-007-2055-2.
[44] A. Migliori, J.L. Sarrao, W.M. Visscher, T.M. Bell, M. Lei, Z. Fisk, R.G. Leisure, Resonant ultrasound spectroscopic techniques for measurement of the elastic moduli of solids, Phys. B Condens. Matter. 183 (1993) 1–24.
[45] S. Nemat-Nasser, M. Obata, A microcrack model of dilatancy in brittle materials, J Appl Mech. 55 (1988) 24–35.
[46] S. Nemat-Nasser, H. Horii, ROCK FAILURE IN COMPRESSION, Int. J. Eng. Sci. 22 (1984) 999–1011.
[47] B. Paliwal, K.T. Ramesh, An interacting micro-crack damage model for failure of brittle materials under compression, J. Mech. Phys. Solids. 56 (2008) 896–923. https://doi.org/10.1016/j.jmps.2007.06.012.
[48] H. Deng, S. Nemat-Nasser, Microcrack Interaction and Shear Fault Failure, Int. J. Damage Mech. 3 (1994) 3–37. https://doi.org/10.1177/105678959400300101.
[49] Z. Hui, L. Hongyan, A Damage Constitutive Model for a Rock Considering the Microcrack Deformation and Propagation, Electron. J. Geotech. Eng. 21 (2016) 4507–4518.
[50] C. Landron, O. Bouaziz, E. Maire, J. Adrien, Experimental investigation of void coalescence in a dual phase steel using X-ray tomography, Acta Mater. 61 (2013) 6821–6829. https://doi.org/10.1016/j.actamat.2013.07.058.
[51] C. Landron, E. Maire, O. Bouaziz, J. Adrien, L. Lecarme, A. Bareggi, Validation of void growth models using X-ray microtomography characterization of damage in dual phase steels, Acta Mater. 59 (2011) 7564–7573. https://doi.org/10.1016/j.actamat.2011.08.046.
[52] F.M. Aben, M.-L. Doan, J.-P. Gratier, F. Renard, Coseismic damage generation and pulverization in fault zones: insights from dynamic Split-Hopkinson Pressure Bar experiments, in: Evol. Fault Zone Prop. Dyn. Process. Seism. Rupture, 2017.

https://www.researchgate.net/profile/Francois_Renard/publication/318172696_Coseismic_Damage_Generation_and_Pulverization_in_Fault_Zones_Evolution_of_Fault_Properties_During_Seismic_Rupture/links/59637e7da6fdccc9b15a3a84/Coseismic-Damage-Generation-and-Pulverization-in-Fault-Zones-Evolution-of-Fault-Properties-During-Seismic-Rupture.pdf (accessed August 8, 2017).

[53] V.L. Shkuratnik, P.V. Nikolenko, A.E. Koshelev, Stress dependence of elastic P-wave velocity and amplitude in coal specimens under varied loading conditions, J. Min. Sci. 52 (2016) 873–877. https://doi.org/10.1134/S1062739116041322.

[54] V.R. Shea, D.R. Hanson, Elastic Wave Velocity and Attenuation as Used to Define Phases of Loading and Failure in Coal, Int. J. Rock Mech. Min. Sci. 25 (1988) 431–437.

[55] B.M.L. Koch, C. Lo, H. Li, T. Sano, J.D. Hogan, Two-Dimensional Dynamic Damage Accumulation in Engineered Brittle Materials, Eng. Fract. Mech. (2020).

[56] C. Lo, T. Sano, J.D. Hogan, Microstructural and mechanical characterization of variability in porous advanced ceramics using X-ray computed tomography and digital image correlation, Mater. Charact. 158 (2019) 109929. https://doi.org/10.1016/j.matchar.2019.109929.

[57] L. Farbaniec, J.D. Hogan, K.Y. Xie, M. Shaeffer, K.J. Hemker, K.T. Ramesh, Damage evolution of hot-pressed boron carbide under confined dynamic compression, Int. J. Impact Eng. 99 (2017) 75–84. https://doi.org/10.1016/j.ijimpeng.2016.09.008.

[58] G. Hu, C.Q. Chen, K.T. Ramesh, J.W. McCauley, Mechanisms of dynamic deformation and dynamic failure in aluminum nitride, Acta Mater. 60 (2012) 3480–3490. https://doi.org/10.1016/j.actamat.2012.03.011.

[59] G. Hu, J. Liu, L. Graham-Brady, K.T. Ramesh, A 3D mechanistic model for brittle materials containing evolving flaw distributions under dynamic multiaxial loading, J. Mech. Phys. Solids. 78 (2015) 269–297. https://doi.org/10.1016/j.jmps.2015.02.014.

[60] C. Poinard, E. Piotrowska, Y. Malecot, L. Daudeville, E.N. Landis, Compression triaxial behavior of concrete: the role of the mesostructure by analysis of X-ray tomographic images, Eur. J. Environ. Civ. Eng. 16 (2012) s115–s136. https://doi.org/10.1080/19648189.2012.682458.

[61] Hy. Li, P. Motamedi, J.D. Hogan, Characterization and mechanical testing on novel (γ + α2) – TiAl/Ti3Al/Al2O3 cermet, Mater. Sci. Eng. A. 750 (2019) 152–163. https://doi.org/10.1016/j.msea.2019.02.039.

[62] B. Amirian, H. Li, J.D. Hogan, The Mechanical Response of a α2(Ti3Al)+γ(TiAl)-Nanograined Al2O3 Cermet Under Dynamic Compression: Modeling and Experiment, Acta Mater. (2019).

[63] C. Lo, T. Sano, J.D. Hogan, Deformation mechanisms and evolution of mechanical properties in damaged advanced ceramics, J. Eur. Ceram. Soc. 40 (2020) 3129–3139. https://doi.org/10.1016/j.jeurceramsoc.2020.02.058.

[64] D.J. Frew, M.J. Forrestal, W. Chen, A split Hopkinson pressure bar technique to determine compressive stress-strain data for rock materials, Exp. Mech. 41 (2001) 40–46.

[65] B. Wattrisse, A. Chrysochoos, J.-M. Muracciole, M. Némoz-Gaillard, Analysis of strain localization during tensile tests by digital image correlation, Exp. Mech. 41 (2001) 29–39. https://doi.org/10.1007/BF02323101.

[66] I.A. Bannikova, O.B. Naimark, S.V. Uvarov, Transition from multi-center fracture to fragmentation statistics under intensive loading, in: Procedia Structural Integrity, 2016: pp. 1944–1950.

[67] H. Horii, S. Nemat-Nasser, Compression-induced Nonplanar Crack Extension, J. Geophys. Res. 87 (1982) 6805–6821.

[68] L.F. Pereira, J. Weerheijm, L.J. Sluys, A new rate-dependent stress-based nonlocal damage model to simulate dynamic tensile failure of quasi-brittle materials, Int. J. Impact Eng. 94 (2016) 83–95. https://doi.org/10.1016/j.ijimpeng.2016.04.002.

[69] D.E. Grady, Adiabatic shear failure in brittle solids, Int. J. Impact Eng. 38 (2011) 661–667. https://doi.org/10.1016/j.ijimpeng.2011.01.001.

[70] K. Hajlaoui, A.R. Yavari, B. Doisneau, A. LeMoulec, W.J. Botta F., G. Vaughan, A.L. Greer, A. Inoue, W. Zhang, å. Kvick, Shear delocalization and crack blunting of a metallic glass containing

nanoparticles: In situ deformation in TEM analysis, Scr. Mater. 54 (2006) 1829–1834. https://doi.org/10.1016/j.scriptamat.2006.02.030.
[71] Z. Rosenberg, D. Yaziv, Y. Yeshurun, S.J. Bless, Shear strength of shock?loaded alumina as determined with longitudinal and transverse manganin gauges, J. Appl. Phys. 62 (1987) 1120–1122. https://doi.org/10.1063/1.339721.
[72] H. Abe, M. Naito, T. Hotta, N. Shinohara, K. Uematsu, Flaw Size Distribution in High-Quality Alumina, J. Am. Ceram. Soc. 86 (2003) 1019–1021.
[73] J. Kim, Y. Kwon, N. Shin, K. Sohn, Visualization of fractures in alumina ceramics by mechanoluminescence, Acta Mater. 53 (2005) 4337–4343. https://doi.org/10.1016/j.actamat.2005.05.032.
[74] E. Strassburger, Visualization of Impact Damage in Ceramics Using the Edge-On Impact Technique, Int. J. Appl. Ceram. Technol. 1 (2004) 235–242.
[75] B.M.L. Koch, P. Jannotti, D. Mallick, B. Schuster, T. Sano, J.D. Hogan, Influence of microstructure on the impact failure of alumina, Mater. Sci. Eng. A. 770 (2020) 138549. https://doi.org/10.1016/j.msea.2019.138549.
[76] L.A. Xue, I.-W. Chen, Deformation and Grain Growth of Low-Temperature-Sintered High-Purity Alumina, J. Am. Ceram. Soc. 73 (1990) 3518–3521. https://doi.org/10.1111/j.1151-2916.1990.tb06489.x.
[77] Y. Zhou, K. Hirao, M. Toriyama, Y. Yamauchi, S. Kanzaki, Effects of intergranular phase chemistry on the microstructure and mechanical properties of silicon carbide ceramics densified with rare-earth oxide and alumina additions, J. Am. Ceram. Soc. 84 (2001) 1642–1644.
[78] D. SCITI, A. BELLOSI, Effects of additives on densification, microstructure and properties of liquid-phase sintered silicon carbide, (n.d.) 7.
[79] H. Manshor, S. Md Aris, A.Z.A. Azhar, E.C. Abdullah, Z.A. Ahmad, Effects of TiO2 addition on the phase, mechanical properties, and microstructure of zirconia-toughened alumina ceramic composite, Ceram. Int. 41 (2015) 3961–3967. https://doi.org/10.1016/j.ceramint.2014.11.080.
[80] E.H. Lutz, M.V. Swain, N. Claussen, Thermal Shock Behavior of Duplex Ceramics, J. Am. Ceram. Soc. 74 (1991) 19–24. https://doi.org/10.1111/j.1151-2916.1991.tb07290.x.
[81] H. Luo, W. Chen, Dynamic Compressive Response of Intact and Damaged AD995 Alumina, Int. J. Appl. Ceram. Technol. 1 (2005) 254–260. https://doi.org/10.1111/j.1744-7402.2004.tb00177.x.
[82] H. Luo, W.W. Chen, A.M. Rajendran, Dynamic Compressive Response of Damaged and Interlocked SiC-N Ceramics, J. Am. Ceram. Soc. 89 (2006) 266–273. https://doi.org/10.1111/j.1551-2916.2005.00688.x.
[83] P. Nicewicz, P. Peciar, O. Macho, T. Sano, J.D. Hogan, Quasi-static confined uniaxial compaction of granular alumina and boron carbide observing the particle size effects, J. Am. Ceram. Soc. 103 (2020) 2193–2209. https://doi.org/10.1111/jace.16871.
[84] E. Krimsky, K.T. Ramesh, M. Bratcher, M. Foster, J.D. Hogan, Quantification of damage and its effects on the compressive strength of an advanced ceramic, Eng. Fract. Mech. 208 (2019) 107–118. https://doi.org/10.1016/j.engfracmech.2019.01.007.
[85] CoorsTek, Advanced Alumina Materials & Manufacturing Processes Brochure, (2016). https://www.coorstek.com/media/1715/advanced-alumina-brochure.pdf.
[86] J.J. Swab, G.D. Quinn, Dynamic Compression Strength of Ceramics: Results from an Interlaboratory Round-Robin Exercise, (2019) 58.
[87] D.J. Frew, M.J. Forrestal, W. Chen, Pulse shaping techniques for testing brittle materials with a split hopkinson pressure bar, Exp. Mech. 42 (2002) 14.
[88] C. Lo, T. Sano, J.D. Hogan, Micostructural and Mechanical Characterization of Variability in Porour Advanced Ceramics Using X-Ray Computed Tomography and Digital Image Correlation, Acta Mater. (2019).
[89] N. Yang, J. Boselli, P.J. Gregson, I. Sinclair, Simulation and quantitative assessment of finite-size particle distributions in metal matrix composites, Mater. Sci. Technol. 16 (2000) 797–805. https://doi.org/10.1179/026708300101508469.

[90] A. Bastawros, Experimental analysis of deformation mechanisms in a closed-cell aluminum alloy foam, J. Mech. Phys. Solids. 48 (2000) 301–322. https://doi.org/10.1016/S0022-5096(99)00035-6.
[91] Analysis of a multiaxial test on a C/C composite by using digital image correlation and a damage model, (n.d.) 11.
[92] B. Pan, K. Qian, H. Xie, A. Asundi, Two-dimensional digital image correlation for in-plane displacement and strain measurement: a review, Meas. Sci. Technol. 20 (2009) 062001. https://doi.org/10.1088/0957-0233/20/6/062001.
[93] W.W. Chen, A.M. Rajendran, B. Song, X. Nie, Dynamic Fracture of Ceramics in Armor Applications, J. Am. Ceram. Soc. 90 (2007) 1005–1018. https://doi.org/10.1111/j.1551-2916.2007.01515.x.
[94] J. Kimberley, J. Paul, A Miniature Tensile Kolsky Bar for Thin Film Testing, in: B. Song, D. Casem, J. Kimberley (Eds.), Dyn. Behav. Mater. Vol. 1, Springer International Publishing, Cham, 2015: pp. 221–226. http://link.springer.com/10.1007/978-3-319-06995-1_33 (accessed October 3, 2016).
[95] M.H. Ahmadi, H. Molladavoodi, A micromechanical Sliding-Damage Model Under Dynamic Compressive Loading, Period. Polytech. Civ. Eng. (2019). https://doi.org/10.3311/PPci.13249.
[96] M. Basista, D. Gross, The sliding crack model of brittle deformation: an internal variable approach, Int. J. Solids Struct. 35 (1998) 487–509.
[97] A. Arab, R. Ahmad, Z.A. Ahmad, Effect of SrCO3 addition on the dynamic compressive strength of ZTA, Int. J. Miner. Metall. Mater. 23 (2016) 481–489. https://doi.org/10.1007/s12613-016-1259-3.
[98] K.T. Ramesh, J.D. Hogan, J. Kimberley, A. Stickle, A review of mechanisms and models for dynamic failure, strength, and fragmentation, Planet. Space Sci. 107 (2015) 10–23. https://doi.org/10.1016/j.pss.2014.11.010.
[99] Z.P. Bažant, F.C. Caner, Impact comminution of solids due to local kinetic energy of high shear strain rate: I. Continuum theory and turbulence analogy, J. Mech. Phys. Solids. 64 (2014) 223–235. https://doi.org/10.1016/j.jmps.2013.11.008.
[100] H. Deng, S. Nemat-Nasser, Microcrack Interaction and Shear Fault Failure, Int. J. Damage Mech. 3 (1994) 3–37. https://doi.org/10.1177/105678959400300101.
[101] Q. Rao, Z. Sun, O. Stephansson, C. Li, B. Stillborg, Shear fracture (Mode II) of brittle rock, Int. J. Rock Mech. Min. Sci. 40 (2003) 355–375. https://doi.org/10.1016/S1365-1609(03)00003-0.

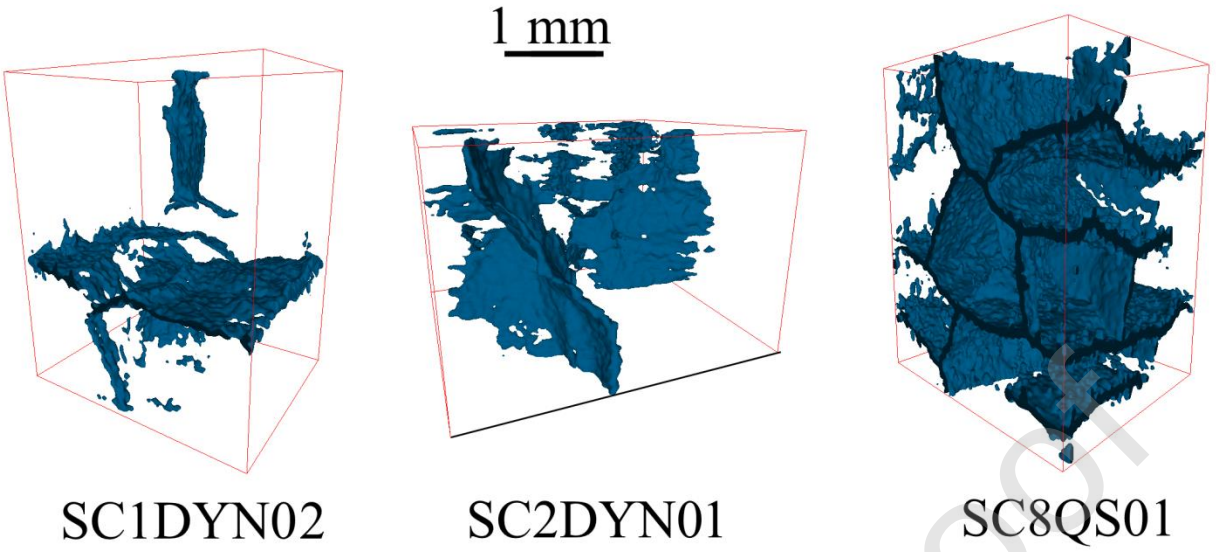

Figure 1– Internal crack reconstructions from X-ray computed tomography for SC1DYN02, SC2DYN01, and SC8QS01 from Lo *et al*.[56] showing the relative evolution of internal cracks. White space is not the absence of cracks but regions where any cracks present are too diffuse to be present in the reconstruction.

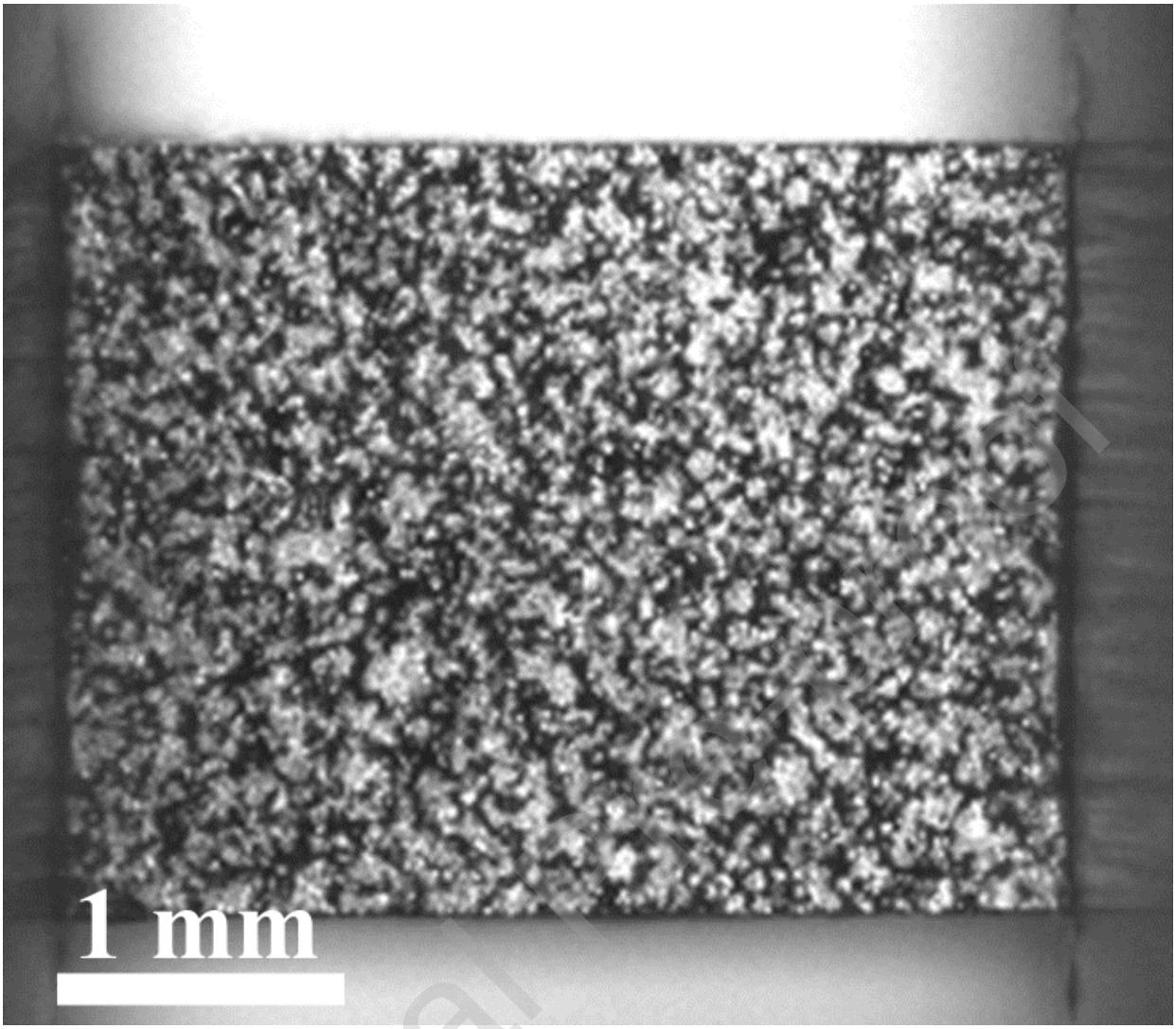

Figure 2 – An example of an AD995 sample sprayed with a speckle pattern for DIC purposes held between the incident and transmitted bars of the Kolsky bar. The field of view in the vertical direction has been cropped in order to better show the features of the sample.

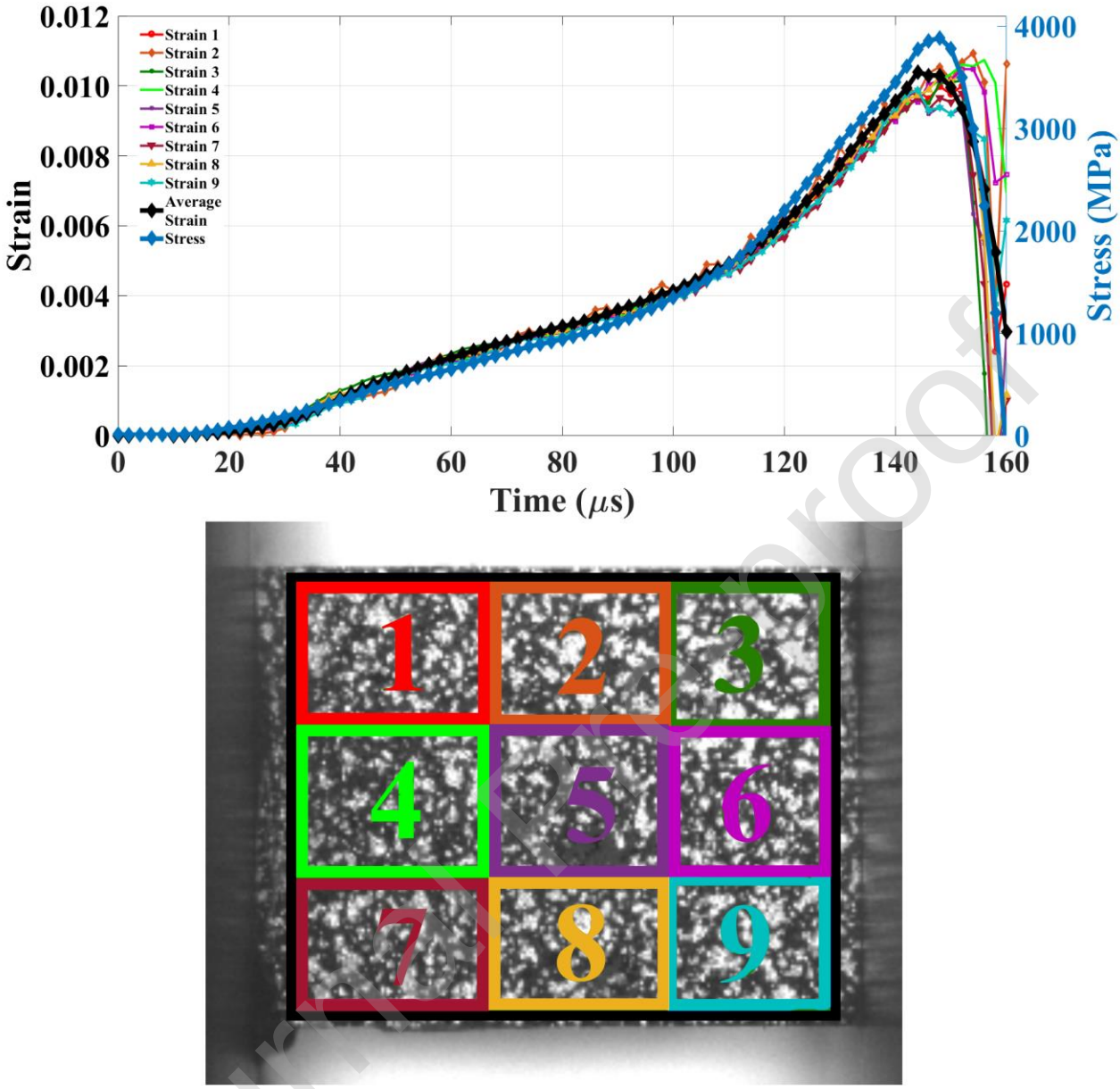

Figure 3 – Combined strain vs. time and stress vs. time plot for SC0DYN02 on the left, and the sample showing the various DIC regions of interest on the right. The average strain vs. time response and the stress vs. time response follow each other and the individual strain responses are not strongly affected by the region, showing that the sample is experiencing good equilibrium.

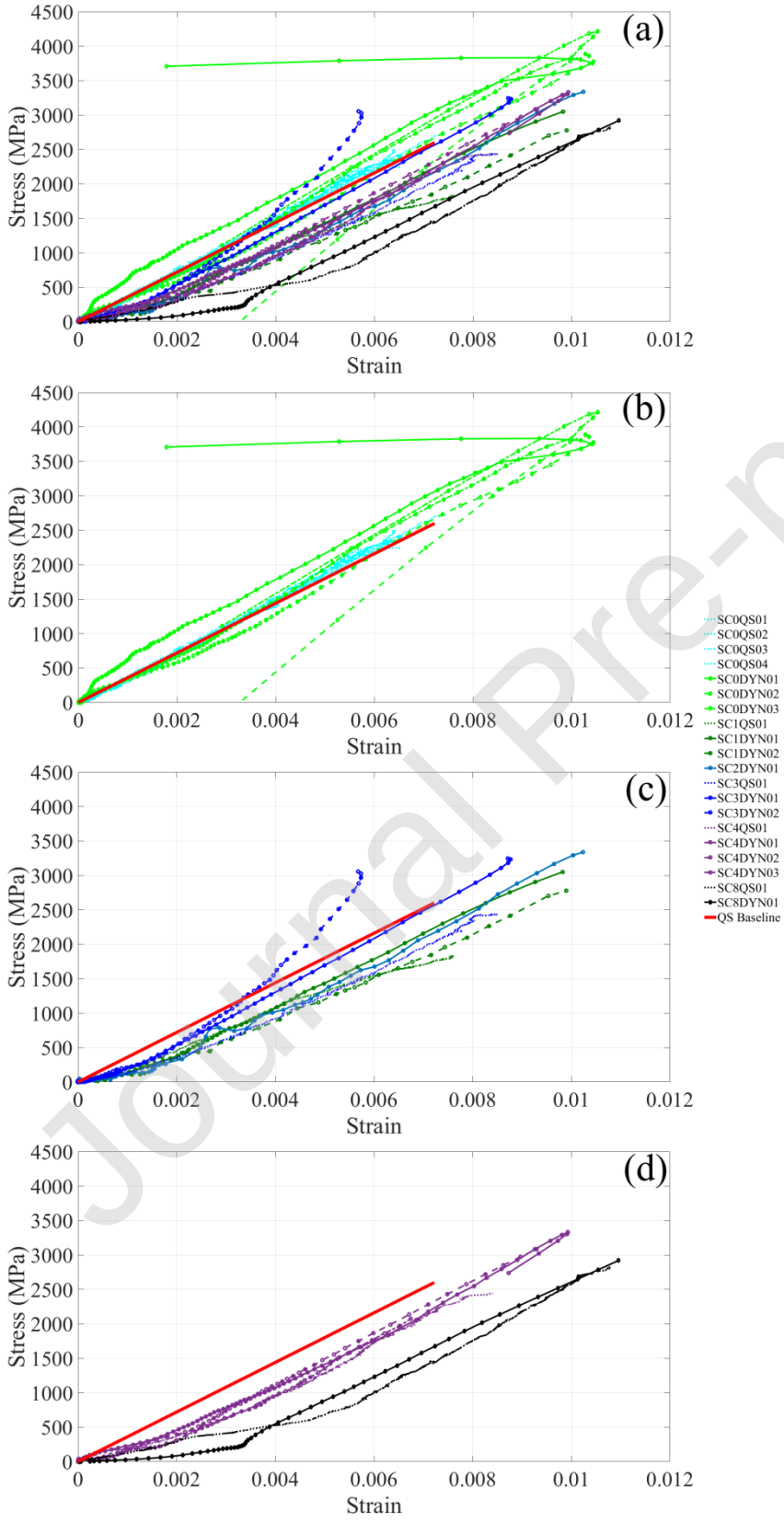

Figure 4 – Stress-strain curves for the various samples tested, showing the variation in early behavior and the eventual convergence towards parallel similar slopes after an initial lower value for damaged samples. Panel (a) shows all tests, panel (b) shows only the tests where no thermal shock cycles were applied, panel (c) has the samples subjected to between 1 and 3 shock cycles, and panel (d) has the samples subjected to 4 and 8 shock cycles. In addition to pristine quasi-static samples, a red line has been added to all sub-figures showing the expected linear elastic behavior based on numerous tests and manufacturer specifications. The three intact dynamic samples show the highest failure stress, as would be expected, but the most damaged samples of SC8QS01 and SC8DYN01 have the highest failure strain, which likely relates to the fact that they had the greatest strain before their slopes became parallel to the rest of the samples. The quasi-static samples all have lower failure strengths and failure strains than the intact samples, but as the number of thermal shock cycles increases the quasi-static samples show an increasing trend in failure strengths and strains. Finally, while the damaged samples fail completely at peak stress and strain, the pristine samples have unloading sections where stress and strain decrease.

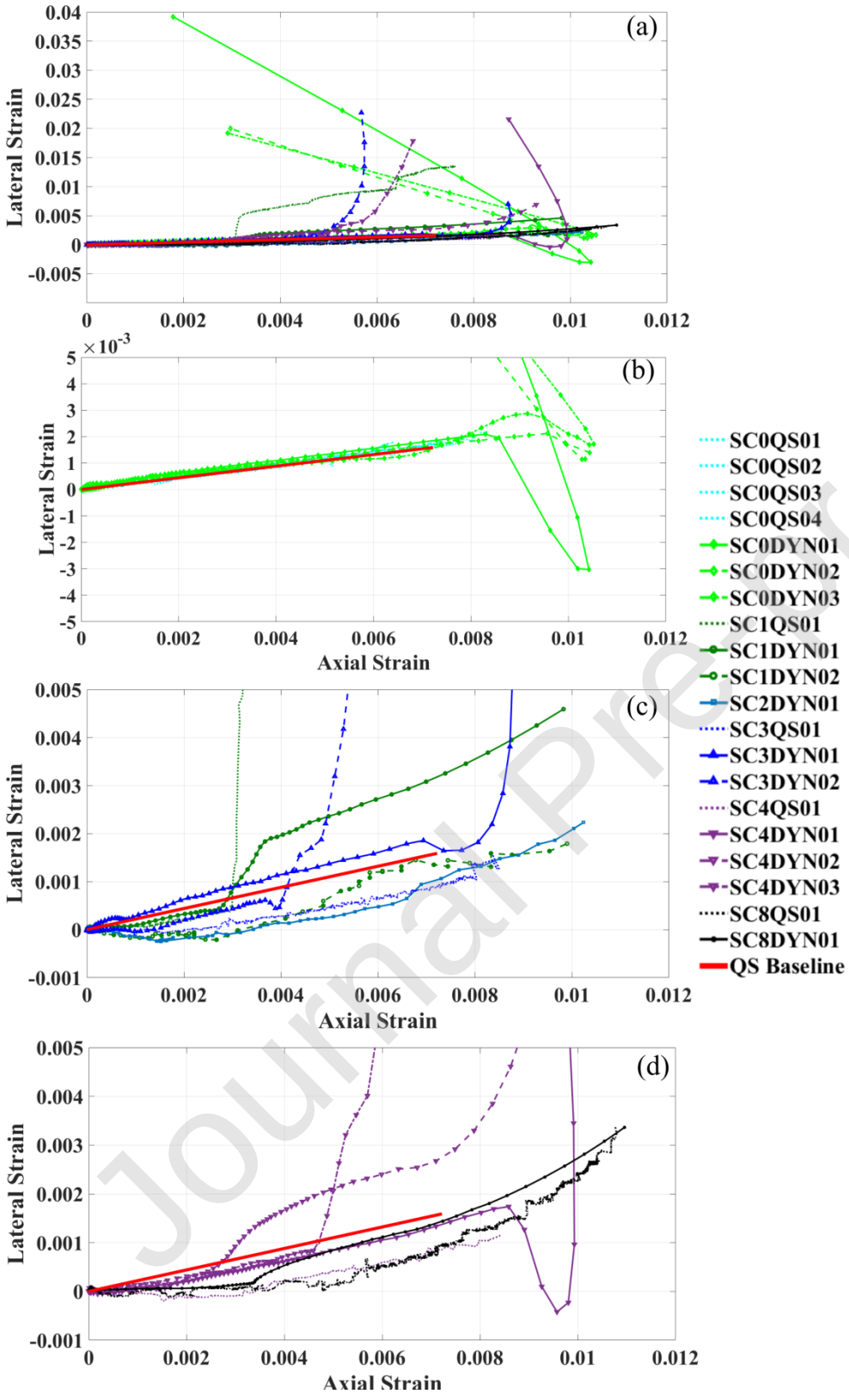

Figure 5 – Lateral vs. axial strain curves for the various samples tested, showing the variation in the ratio between the two strains. Panel (a) shows all tests, panel (b) shows only the tests where no thermal shock cycles were applied, panel (c) has the samples subjected to between 1 and 3 shock cycles, and panel (d) has the samples subjected to 4 and 8 shock cycles. In addition to pristine quasi-static samples, a red line has been added to all sub-figures showing the expected linear elastic behavior based on numerous tests and manufacturer specifications. Highly damaged samples abruptly fail, while the less damaged samples show large increases in lateral strain before failure. The pristine samples, SC4DYN01 and SC3DYN02 on the other hand show unloading behavior alongside these large increases in lateral strain.

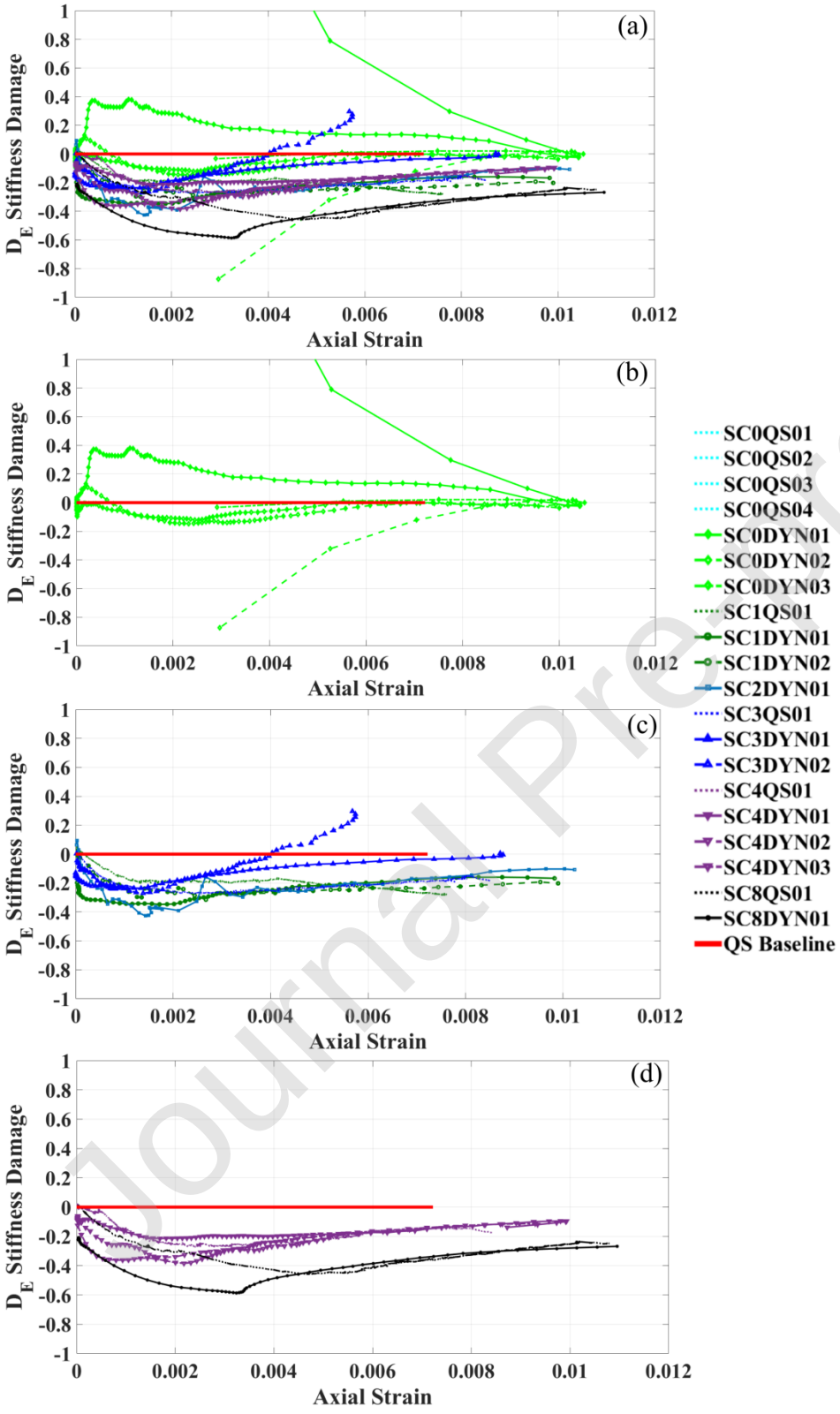

Figure 6 – D_E stiffness damage versus axial strain. Panel (a) shows all tests, panel (b) shows only the tests where no thermal shock cycles were applied, panel (c) has the samples subjected to between 1 and 3 shock cycles, and panel (d) has the samples subjected to 4 and 8 shock cycles. A red line has been added to all images showing the expected linear elastic behavior based expected failure strain with no damage before failure. Pristine quasi-static lines are obscured by the baseline quasi-static line, which captures their behavior. Seen is that all of the samples start with low effective stiffness before recovering towards their quasi-static pristine value ($D_E = 0$) before plateauing at some value, with the exception of SC3DYN02 and SC0DYN01, which show stiffness greater than its quasi-static value at failure. Of particular interest is the fact that this convergence towards quasi-static pristine also holds for the pristine samples, even if they begin higher than pristine such as SC0DYN01 and SC0DYN02.

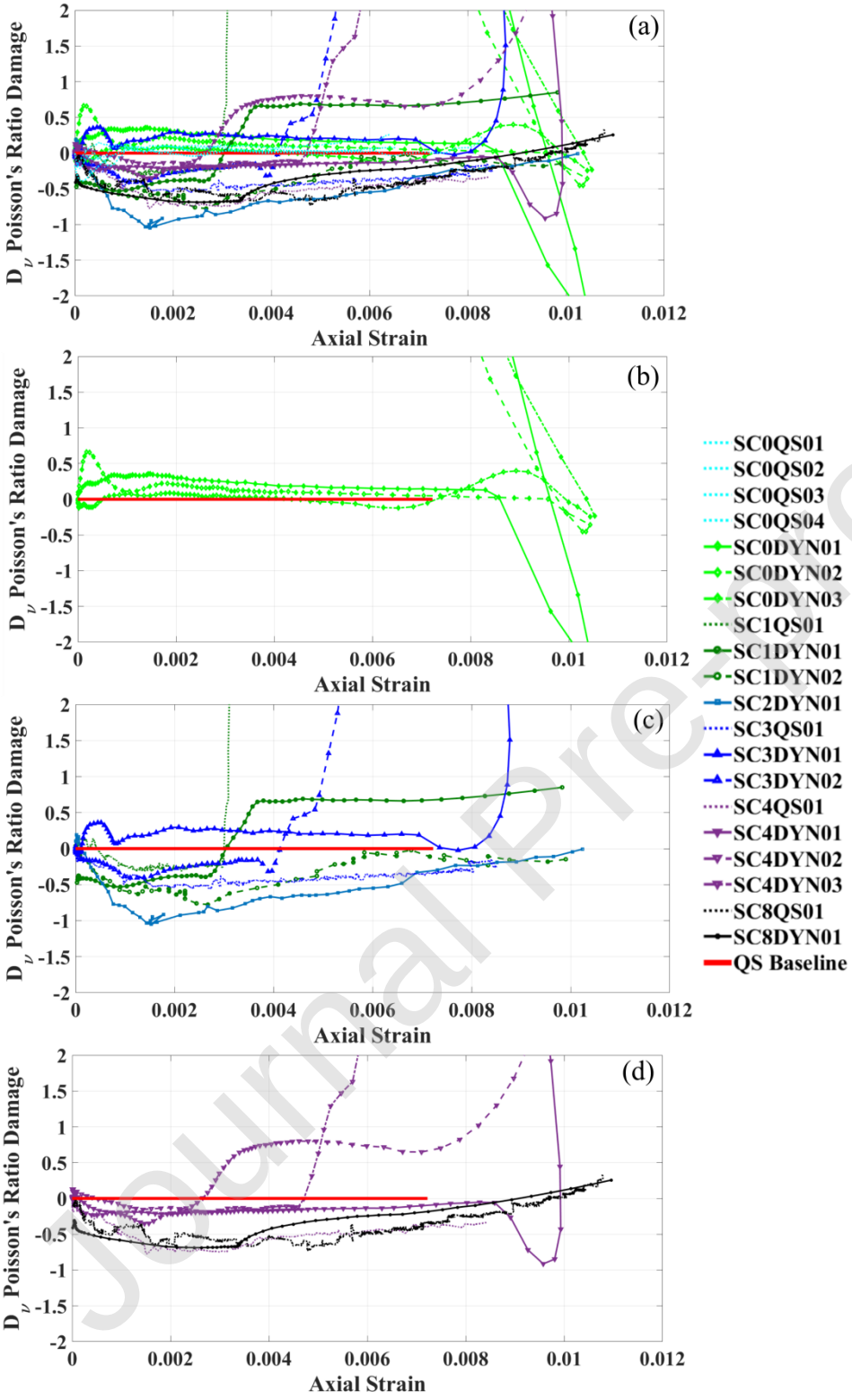

Figure 7 - D_ν Poisson's ratio damage versus axial strain. Panel (a) shows all tests, panel (b) shows only the tests where no thermal shock cycles were applied, panel (c) has the samples subjected to between 1 and 3 shock cycles, and panel (d) has the samples subjected to 4 and 8 shock cycles. A red line has been added to all images showing the expected linear elastic behavior to failure strain with no damage before failure. Pristine quasi-static lines are obscured by the baseline quasi-static line, which captures their behavior. The image shows a wide variability in the behaviors, in comparison to

Figure 6, which shows a more consistent set of behaviors. However, as before the less damaged samples, including the pristine samples, demonstrate large increases in mechanical damage during failure.

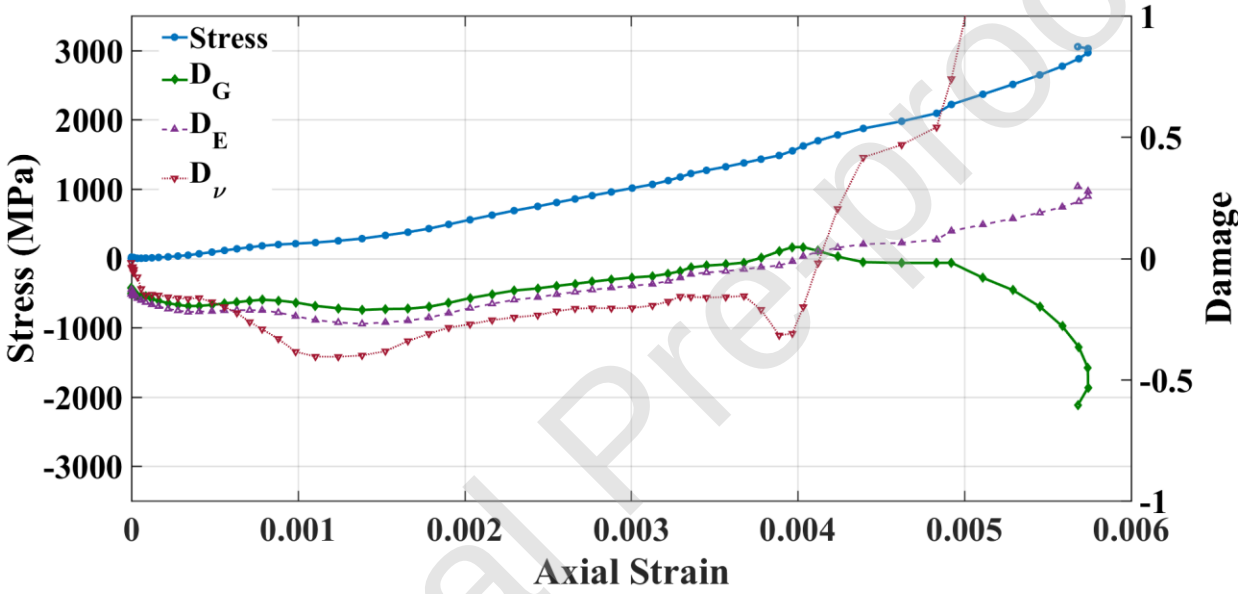

Figure 8 – Stress (left axis) and damage measures (right axis) vs. axial strain for SC3DYN02. Damage measures track apparent changes in Young's modulus (E), Poisson's ratio (ν), and shear modulus (G). While the sample shows an increasing Young's modulus while loaded, including a final apparent Young's modulus 25% greater than pristine quasi-static, it is the shear modulus where the actual damage appears most prominently.

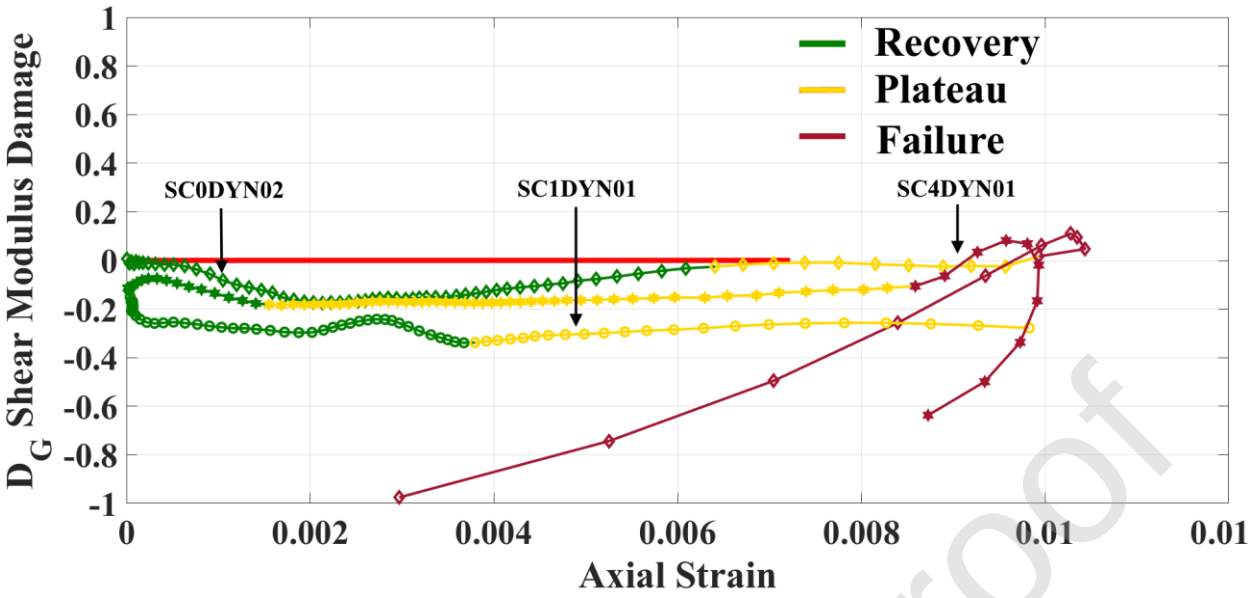

Figure 9 - D_G shear modulus damage vs. axial strain for SC0DYN02, SC1DYN01, and SC4DYN01 showing the different behavioral stages separated by color. The first stage, *recovery*, is in green and features an initial decline in apparent shear modulus, before either returning to D_G for SC0DYN02 or assuming a consistent state for SC1DYN01 and SC4DYN01. The second stage in yellow is the *plateau stage*, wherein the D_G value remains near constant as axial strain increases. The third stage is in red and is the *failure stage*, wherein the value of D_G begins to rapidly change with axial strain, including axial strain decreasing. In this figure only SC0DYN02 and SC4DYN01 demonstrate a *failure stage*, with SC1DYN01 suffering catastrophic fragmentation at the end of its *plateau stage* and thus losing correlation.

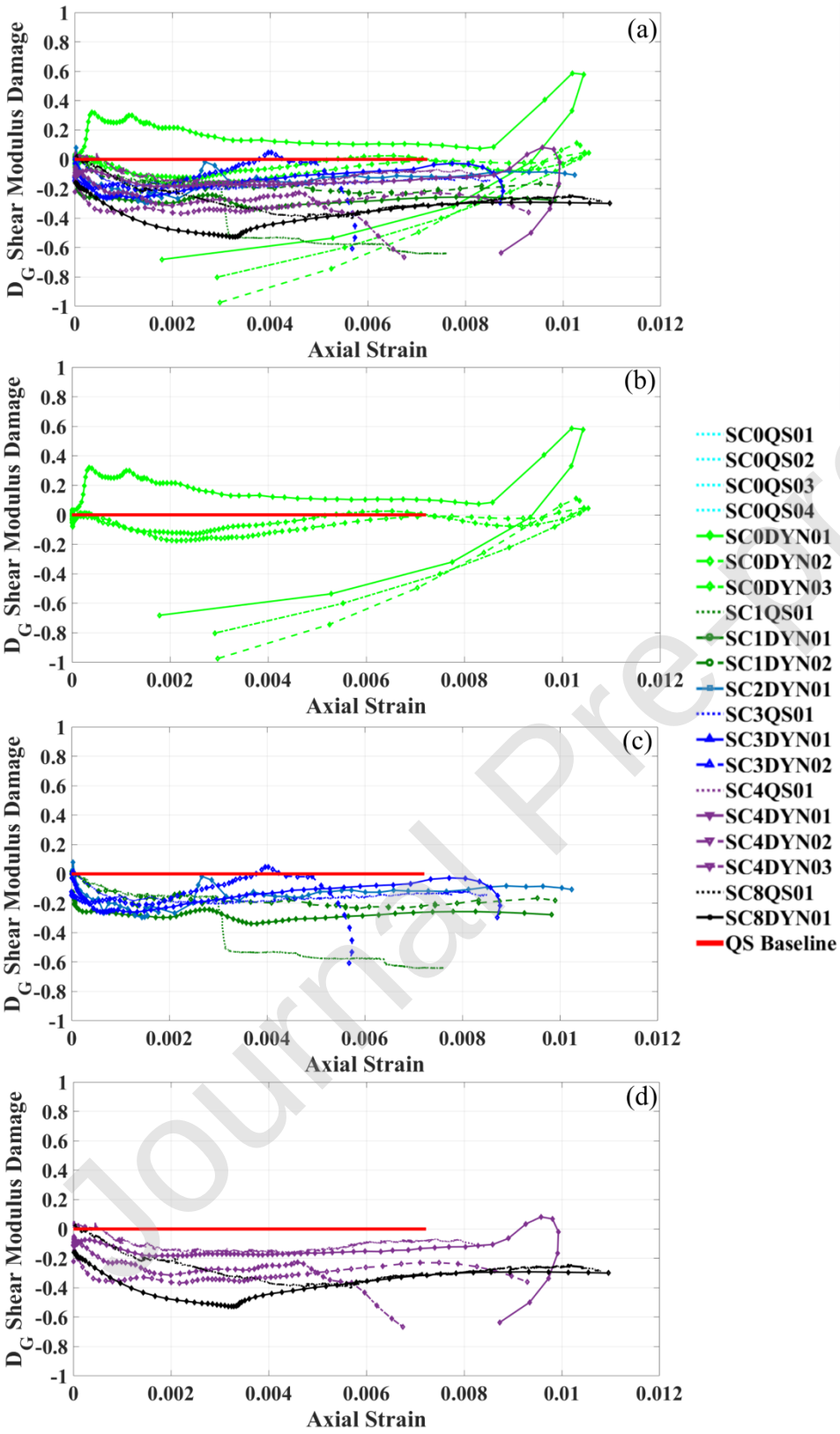

Figure 10 - D_G shear modulus damage for all samples. Panel (a) shows all tests, panel (b) shows only the tests where no thermal shock cycles were applied, panel (c) has the samples subjected to between 1 and 3 shock cycles, and panel (d) has the samples subjected to 4 and 8 shock cycles. A red line has been added to all images showing the expected linear elastic behavior to failure strain with no damage before failure. Pristine quasi-static lines are obscured by the baseline quasi-static line, which captures their behavior. The image shows that shear modulus damage is consistently negative at failure, even when materials such as SC0DYN01 exhibits an apparent increase in Young's modulus before failure. In this way of showing the data physical damage primarily manifests as a reduction in the capacity for the sample to tolerate shear damage before fracture.

Tables

Table 1 – Key data on damaged samples tested, with the number of thermal shock cycles and the failure strength and failure strain when subjected to compression.

Name	Thermal Cycles	Failure Strength (GPa)	Failure Strain (%)
QS Baseline	0	2.60	0.72
SC0QS01	0	2.73	0.75
SC0QS02	0	2.60	0.64
SC0QS03	0	2.42	0.66
SC0QS04	0	2.25	0.65
SC0DYN01	0	3.91	1.00
SC0DYN02	0	3.74	1.00
SC0DYN03	0	4.06	1.05
SC1QS01	1	1.83	0.76
SC1DYN01	1	3.01	0.98
SC1DYN02	1	2.78	1.00
SC2DYN01	2	3.33	1.02
SC3QS01	3	2.43	0.83
SC3DYN01	3	3.30	0.91
SC3DYN02	3	3.10	0.63
SC4QS01	4	2.43	0.84
SC4DYN01	4	3.39	1.03
SC4DYN02	4	3.09	0.92
SC4DYN03	4	2.07	0.67
SC8QS01	8	2.82	1.08
SC8DYN01	8	3.17	1.08